Colour–magnitude diagrams of transiting Exoplanets – II. A larger sample from photometric distances

Amaury H. M. J. Triaud,[1][★][†] Audrey A. Lanotte,[2] Barry Smalley[3] and Michaël Gillon[2]

[1]*Kavli Institute for Astrophysics & Space Research, Massachusetts Institute of Technology, Cambridge, MA 02139, USA*
[2]*Institut d'Astrophysique et de Géophysique, Université de Liège, Allée du 6 Août 17, Sart Tilman, B-4000 Liège 1, Belgium*
[3]*Astrophysics Group, Keele University, Staffordshire ST5 5BG, UK*

ABSTRACT

Colour–magnitude diagrams form a traditional way of presenting luminous objects in the Universe and compare them to each other. Here, we estimate the photometric distance of 44 transiting exoplanetary systems. Parallaxes for seven systems confirm our methodology. Combining those measurements with fluxes obtained while planets were occulted by their host stars, we compose colour–magnitude diagrams in the near and mid-infrared. When possible, planets are plotted alongside very low mass stars and field brown dwarfs, who often share similar sizes and equilibrium temperatures. They offer a natural, empirical, comparison sample. We also include directly imaged exoplanets and the expected loci of pure blackbodies. Irradiated planets do not match blackbodies; their emission spectra are not featureless. For a given luminosity, hot Jupiters' daysides show a larger variety in colour than brown dwarfs do and display an increasing diversity in colour with decreasing intrinsic luminosity. The presence of an extra absorbent within the 4.5 μm band would reconcile outlying hot Jupiters with ultra-cool dwarfs' atmospheres. Measuring the emission of gas giants cooler than 1000 K would disentangle whether planets' atmospheres behave more similarly to brown dwarfs' atmospheres than to blackbodies, whether they are akin to the young directly imaged planets, or if irradiated gas giants form their own sequence.

Key words: planets and satellites: atmospheres – binaries: eclipsing – brown dwarfs – stars: distances – Hertzsprung–Russell and colour–magnitude diagrams – planetary systems.

It is trivial to convert fluxes measured at occultation, or obtained while observing the phase curves of transiting exoplanets into absolute magnitudes. One only needs a distance measurement. Two colour–magnitude diagrams for transiting – or occulting – exoplanets were presented in Triaud (2014) for seven systems that have *Hipparcos* parallaxes (van Leeuwen 2007). Coincidentally, this happened approximately a century after the first Hertzsprung–Russell diagrams were composed (Hertzsprung 1911; Russell 1914a,b,c).

Colour–magnitude diagrams offer a means to compare exoplanets with each other, using natural units for observers. In addition, they allow one to infer global properties without requiring the need to fit complex atmospherical models through the sparse data points that can only be gathered at this stage. Those inferences can be made by comparing exo-atmospheres to other objects having similar temperatures and sizes; very low mass stars and field brown dwarfs are a readily available and well-studied sample. Young, directly imaged planets are routinely compared to field brown dwarfs for this very reason (e.g. Bonnefoy et al. 2013). Finally, irradiated and non-irradiated gas giants can be compared to each other in colour–magnitude space. Those diagrams can offer a tool to pinpoint the processes that lead highly irradiated planets to be bloated (e.g. Demory & Seager 2011).

Just as the construction of the Hertzsprung–Russell diagram led to vast advances in stellar formation and evolution, the compilation of colour–magnitude diagrams for transiting exoplanets will likely spur similar developments. Models in colour space may predict that different planet families have distinct locations or sequences (dependent on their gravity, their atmospheric structure, their relative abundances, etc.). This would provide diagnostics to select suitable targets for further follow-up, in a fashion similar to selecting a particular stellar population, for instance, to remove giant contaminants prior to a survey focusing on G and K dwarfs. In the case of irradiated gas giants specifically, the lack of cloud cover may cause objects to fall in a specific region in colour space. Being identifiable, it will help optimize the detection of atmospheric features

---

★ E-mail: triaud@mit.edu
† Fellow of the Swiss National Science Foundation.

in transmission. In addition, if planets follow defined sequences, magnitudes obtained in one band lead to accurate predictions for others bands. It can only encourage observations at wavelengths more difficult to obtain.

In total, 44 systems (43 planets and 1 brown dwarf) have been observed at occultation and were present in the literature. Rather than waiting for *Gaia* (e.g. Perryman et al. 2001) to deliver its much awaited parallaxes, this paper will instead use photometric distances. Thanks to their transiting configurations and to the intensive observational efforts that have been undertaken both in the confirmation and in the characterization of these objects, the fundamental stellar parameters are accurately known. This means that reliable distances can be computed such as was done for example by Torres et al. (2008). Hertzsprung–Russell diagrams can be represented as luminosity versus effective temperature. We instead opted for using colours instead of temperatures (Beatty et al. 2014), because magnitudes are closer to direct observables.

The paper is organized in the following way: we first outline our procedure to measure photometric distances (Section 1) and then describe how the host stars' apparent magnitudes were determined from the *Spitzer* photometry (Section 2). In the following section, different colour–magnitude diagrams are drawn and described in qualitative and quantitative ways. We then discuss our results and conclude.

1 THE DETERMINATION OF PHOTOMETRIC DISTANCES

Our distances are derived from catalogued parameters: we obtained effective temperatures ($T_{\rm eff}$), surface gravities (log g) and metallicities ([Fe/H]) from TEPCAT[1] (Southworth 2011) and used those to compute stellar radii ($R_\star$) thanks to a relation provided in Torres, Andersen & Giménez (2010, Chapter 8). $R_\star$ and $T_{\rm eff}$ directly lead to stellar luminosities ($L_\star$) that were in turn converted into bolometric magnitudes ($M_{\rm bol}$) using the following relation (Cox 2000):

$$M_{\rm bol} = 4.75 - 2.5 \log L_\star. \tag{1}$$

Absolute visual magnitudes (M_V) were estimated thanks to bolometric corrections estimated by Flower (1996); values are provided in Table B2.

We explored the Tycho2 catalogue (Høg et al. 2000) to compile a list of apparent visual magnitude m_V. Failing to find a number of systems we turned to APASS/UCAC4 (Zacharias et al. 2013) and then to TASS (Droege et al. 2006). Distances were obtained from the distance modulus ($m_V - M_V$). Errors are propagated throughout.

No reddening corrections, $E(B - V)$, were applied since they are not available for most of our sample. We expect most $E(B - V) <$ 0.1, leading to offsets $A_V < 0.33$ on ($m_V - M_V$) (Maxted, Koen & Smalley 2011).

The distances we calculated are given in Table B2 and are visually represented in Fig. 1. Those plots show our results compared to corresponding distances from the revised *Hipparcos* catalogue (van Leeuwen 2007). We also compare our estimates to photometric distances from Torres et al. (2008), which provides a wider range and greater overlap of systems than *Hipparcos*. Our two most discrepant distance measurements are on GJ 436 and GJ 1214. This is most probably caused by the late type of both stars, who, with masses <0.6 M$_\odot$, fall outside the range over which the Torres relation has

been calibrated for. We thus adopt the most recent distance estimates, from van Leeuwen (2007) and from Anglada-Escudé et al. (2013), respectively. Removing those two objects, the reduced χ_r^2 for Fig. 1(b) changes from 2.7 ± 0.8 to 0.6 ± 0.4. All comparisons lead to reduced $\chi_r^2 \sim 1$. Reddening is thus contained within our error bars.

2 THE DETERMINATION OF *SPITZER* APPARENT MAGNITUDES

The *WISE* satellite (Cutri & et al. 2012) has two bandpasses, W1 and W2, that resemble two of *Spitzer*'s InfraRed Array Camera (IRAC) channels. Kirkpatrick et al. (2011) showed the colour agreement between both spacecraft, on field brown dwarfs. Needing to use the IRAC 3 and 4, for which there is no *WISE* equivalent, we derived photometry from all *Spitzer* channels and compared the [3.6] and [4.5] to W1 and W2, to validate our measurements in the redder channels.

We searched the *Spitzer* Heritage Archive[2] for all frames obtained on the targets with reported occultations in the published literature (Table B4). Apparent magnitudes were obtained for each set of observations. Our methods for extracting the photometry are located in Appendix A, and here summarized. We perform aperture photometry on the IRAC images calibrated by the standard *Spitzer* pipeline according to the EXOPHOT PYRAF pipeline following Lanotte et al. (in preparation). Stellar flux is corrected for contribution from visual companions, if relevant. We average those flux and convert them into Vega apparent magnitudes following the methods described by Reach et al. (2005). When several observations were made of the same stars, we computed the optimal average of their apparent magnitude in each of *Spitzer*'s Astronomical Observation Request (AOR) to produce the values located in Table B2.

Our estimates are graphically compared in Fig. 2 to corresponding bands employed by the *WISE* satellite. Reduced χ_r^2 are calculated. They indicate very good agreement between both set of values. Despite good agreement some objects are clearly discrepant. For example CoRoT-2A, that is ~0.3 mag fainter in our estimation. We suspect this is because *WISE* could not distinguish CoRoT-2A from its visual companion, as we have done when deconvoluting. In the 4.5 μm band, objects brighter than the 6$^{\rm th}$ magnitude are also discrepant. For those removed, χ_r^2 drops from 1.7 to 0.4. All our bright targets remained well within IRAC 2's region of linearity. The discrepancy likely emanates from *WISE*. Our values can therefore be considered as being more accurate. The low χ_r^2 we obtain reveals that we probably overestimate our error bars. We assume the same of the IRAC 3 and 4 channels and use our apparent magnitudes to compute those of planets.

3 COLOUR–MAGNITUDE DIAGRAMS

Planet-to-star flux ratios, measured at occultation in the *J*, *H* and *K* bands as well as observed by *Spitzer*'s IRAC 1, 2, 3 and 4 bands, were obtained from the literature and transformed into a change in magnitude. Using stellar apparent magnitudes (Table B2), planetary fluxes were thus transformed into apparent magnitudes (Table B4). Although only a technicality, this step is interesting in immediately providing an estimate of whether a certain instrument, or mirror size, is sufficient to detect a given planet. In this way, we realize that

---

[1] www.astro.keele.ac.uk/jkt/tepcat/

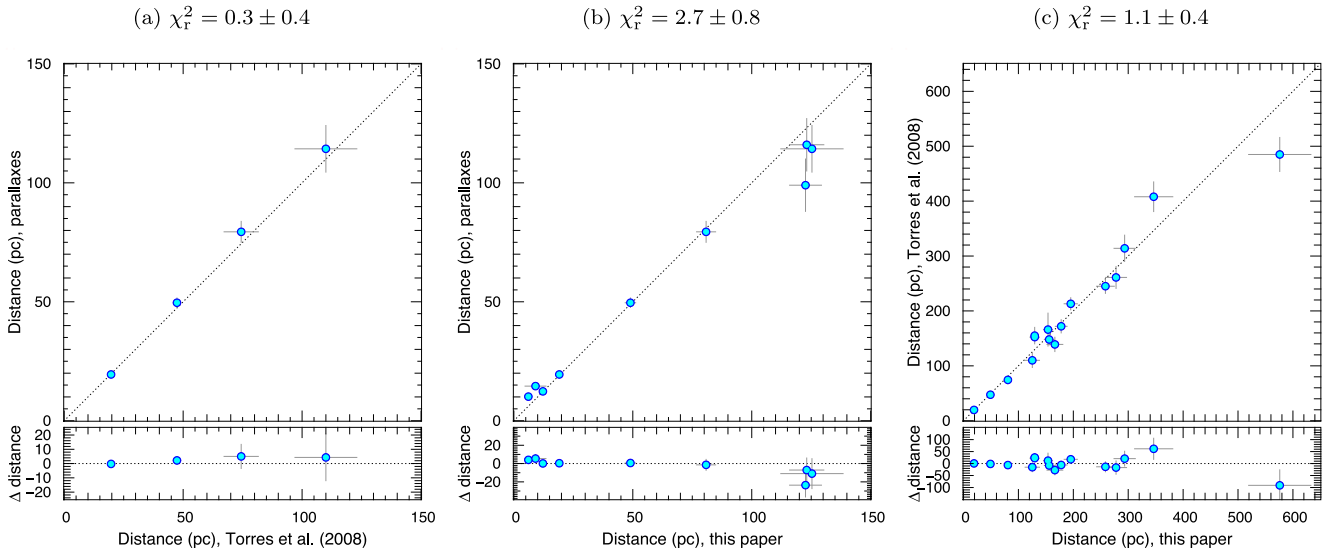[2] http://sha.ipac.caltech.edu/applications/Spitzer/SHA/

Figure 1. Distance measurements compared with one another, from our sample, including the two discrepant stars GJ 436 and GJ 1214. Reduced χ_r^2 are given. (a) Parallactic distances from *Hipparcos* versus photometric distances from Torres, Winn & Holman (2008). (b) Parallactic distances from *Hipparcos* versus photometric distances estimated in this paper. (c) Photometric distances from Torres et al. (2008) versus photometric distances estimated in this paper.

55 Cnc e, a rocky planet, is a 14th magnitude at 4.5 μm, meaning it can be detectable with a medium-size telescope, which it was (Demory et al. 2012). This is also a practical way to compare transiting planets with directly detected planets. Using our computed distance moduli (Table B2), we obtain absolute magnitudes for stars and planets, which are listed, respectively, in Tables B3 and B5.

The planets' absolute magnitudes are represented by circular, blue symbols arranged as colour–magnitude diagrams in Figs 3 and 4. We will now describe how planets are spread with respect to each other but also to ultra-cool dwarfs. Very low mass stars and brown dwarfs are represented in the background of the same diagrams as diamonds whose colours move from orange to black as a function of their assigned spectral type (ranging from M5 to Y1).

3.1 Comparing with ultra-cool dwarfs

Information comes from comparing a new sample to one already well studied or to a model. Since models for irradiated planets are yet to be computed for colour space, very low mass stars and field brown dwarfs, which have similar effective temperatures and sizes, come as a readily available comparison sample. We can now see if planets follow or depart from the known location of those objects. Our comparison sample was borrowed from Dupuy & Liu (2012), who recently compiled a vast list of ultra-cool dwarf magnitudes and parallaxes. Later in the paper, a comparison will be made to the expected location of blackbodies (Section 4) and to the position of directly detected planets (Fig. 5).

Ultra-cool dwarfs comprise very late M dwarfs and brown dwarfs. They span the M, L, T and Y spectral classes. The distinction between the M, L and T spectral classes is described by Kirkpatrick (2005), while the Y class is defined in Cushing et al. (2011). Covering effective temperatures ranging from roughly 2500 to 1300 K, the L-dwarf sequence is identified by the disappearance of TiO and VO absorption as those species and others condensate into dust clouds that are thickening with decreasing temperatures, causing an accrued reddening. A rapid blueward change in near-infrared colours for objects with similar effective temperature outlines the transition between spectral classes L7 to T4 (Fig. 3). This colour variation is

interpreted as the disappearance of suspended dust from the photosphere. The process through which these condensates of atomic and molecular species vanish is the scene of very active research. Tsuji (2002), Marley et al. (2002) and Knapp et al. (2004) proposed that as the atmosphere cools, it reaches a temperature at which dust sedimentation efficiency increases dramatically producing a drain of the cloud decks via a 'sudden downpour'. Ackerman & Marley (2001) and Burgasser et al. (2002) instead proposed that, very much like what can be observed on Jupiter where clouds are discretized in separate bands, brown dwarfs' silicate clouds could fragment and progressively reveal the deeper, hotter regions of the atmosphere. This scenario produces clear signatures, such as photometric variability caused by inhomogeneous structures rotating in and out of view. Those are being detected on an increasing number of brown dwarfs (Artigau et al. 2009; Radigan et al. 2012, 2014; Heinze et al. 2013), with some contention which spectral types are more likely to vary and about what causes variability (Wilson, Rajan & Patience 2014). One could also expect near-stochastic modulations like as has been noticed on Luhman-16B by Gillon et al. (2013). Further observations confirmed the presence of patchy clouds on Luhman-16B (Crossfield et al. 2014). From spectral type T5 and beyond, atmospheres are thought to be clear and continue to cool down. T dwarfs have effective temperatures between 1500 and ~600 K. The transition to the Y class is defined by the appearance of ammonia and the disappearance of alkali lines produced by the condensation of sodium and potassium.

Interestingly, transiting planets, most often hot Jupiters, have dayside magnitudes, brightness temperatures and colours that overlap with the entire ultra-cool dwarf range. For instance, WASP-12Ab, the intrinsically brightest planet in the current sample, is as hot as an M6 dwarf. Its inferred size is as large as a $0.16\,\mathrm{M_\odot}$ star (Baraffe et al. 1998). This would allow in principle to draw parallels between planets and ultra-cool dwarfs, especially so, since mass regimes of field brown dwarfs and extrasolar planets are overlapping (Latham et al. 1989; Chauvin et al. 2004; Caballero et al. 2007; Deleuil et al. 2008; Marois et al. 2008; Hellier et al. 2009; Sahlmann et al. 2011; Siverd et al. 2012; Delorme et al. 2013; Díaz et al. 2013; Naud et al. 2014).
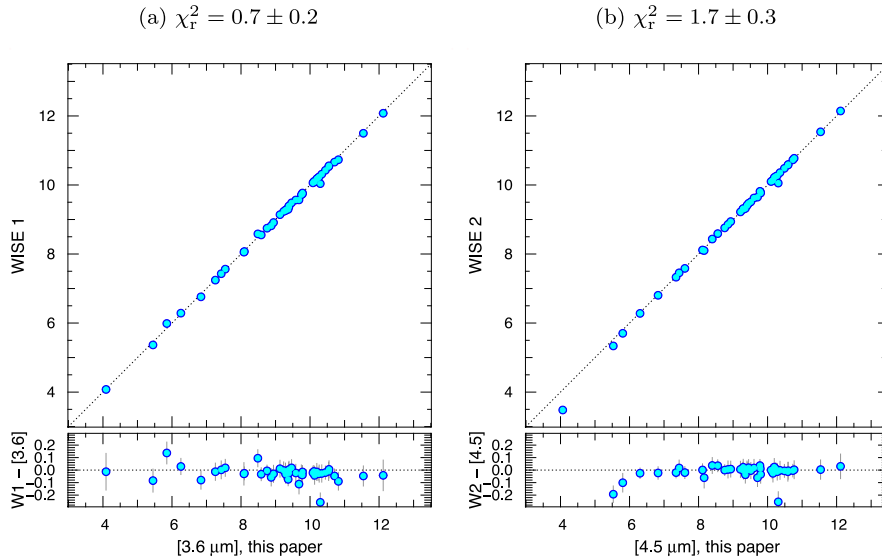
(a) $\chi_r^2 = 0.7 \pm 0.2$

(b) $\chi_r^2 = 1.7 \pm 0.3$

Figure 2. Apparent magnitude measurements comparing those obtained by *WISE* to those that we estimated, from the *Spitzer* images. CoRoT-2A is clearly discrepant in both, because it is blended with CoRoT-2B the *WISE* data. Reduced χ_r^2 are given; (a) on a band centred around 3.6 μm; (b) on a band centred around 4.5 μm. The discrepant point at ~10.3 is the CoRoT-2 system. Objects >6th magnitude appear brighter in the *WISE* 2 band, which may be due to some detector effects. Discrepant points removed, $\chi_r^2 < 1$.

3.2 Near-infrared

The *J, H* and K_S bands' colour–magnitude diagrams contain a large number of field brown dwarfs (see Dupuy & Liu 2012 and references therein) but very few planets. Each of Fig. 3's panels contains WASP-12Ab, the only planet with firm detections of its emission in each of those near-infrared bands ($M_J = 9.42$, $M_H = 8.83$, $M_{K_s} = 8.16$). A few more measurements were obtained on individual systems, but often in only one band (depicted as dotted lines). WASP-12Ab's location seems to agree well with the top of the ultra-cool dwarf distribution especially in the $J - H$ colour. The two colours involving the K_S band would imply that the object is redder than most late M dwarfs. However, a recent work by Rogers et al. (2013) showed that eclipse depth measurements, notably in the K_S bandpass, are likely to be biased towards deeper values. This in turn would make authors infer brighter planets, leading to a smaller magnitude and a redder colour index. Bean et al. (2013) observed WASP-19b at low spectral resolution and consistently found shallower occultation depths than broad-band measurements would imply.

It remains unclear whether irradiated planetary atmosphere should follow the same general behaviour that very low mass stars and field brown dwarfs have, whether they would constitute their own sequence or agree with a blackbody (see Section 4 for a discussion on the matter). If indeed, irradiated planets and ultra-cool dwarfs were to coincide, then positioning a new measurement in a colour–magnitude diagram will become an efficient method to verify anyone's results. For instance, it can immediately be noticed how most K_S bands results imply redder colours than would otherwise be anticipated.

By extension, obtaining a detection in one band would offer straightforward predictions for the other two bands. As an example, WASP-19b has an absolute magnitude in the *H* band, $M_H = 9.80 \pm 0.21$ (Table B5). Reading on the M_H versus $J - H$ plot, we notice that its magnitude intersects with the M- and L-dwarf sequence at $J - H = 0.6 \pm 0.1$. This leads to $M_J = 10.40 \pm 0.23$, which we can convert into an apparent magnitude. WASP-19b can

be predicted to have $m_J = 17.60 \pm 0.21$, on a par with WASP-12Ab's measurement (Table B4).

3.3 Mid-infrared

In the mid-infrared, all the bands that were considered are the *Spitzer*'s IRAC channels. Both ultra-cool dwarfs and exoplanets have been observed extensively, especially so in the IRAC 1 and 2 centred at 3.6 and 4.5 μm. Compared to the seven systems presented in Triaud (2014), the first diagrams in the top two rows in Fig. 4 show a marked increase in the number of objects.

3.3.1 [3.6]−[4.5]

The M- and L-dwarf sequence is colourless in those bands. Objects get fainter for decreasing temperatures. As brown dwarfs transition towards the T sequence, a sharp turn occurs, caused by the widening and deepening methane absorption band at 3.3 μm, revealed by the recession of dust clouds in brown dwarfs' atmospheres (e.g. Patten et al. 2006, and references therein). This leads to increasingly redder colours with increasing magnitudes. The clarity of this pattern is handy to compare planets and brown dwarfs together. So far no planet that has had its emission detected clearly falls within the T range. Good contenders can be found in HAT-P-12b (Hartman et al. 2009) whose upper limit places it beyond the methane *kink* and in WASP-80b that has a reported effective temperature around 800 K (Triaud et al. 2013b; Mancini et al. 2014). All currently measured hot Jupiters can therefore be compared to the M and L sequence (GJ 436b, a Neptune, is kept aside for now).

Despite significant scatter, one can notice that objects are not located completely at random. No object redder than [3.6]−[4.5] = 1 for example exists. All planets but two have colours compatible or redder than brown dwarfs. This gets clearer for absolute magnitudes in the redder channels. Only GJ 436b ([3.6]−[4.5] < 0.6) and WASP-8Ab ([3.6]−[4.5] = 0.6) are significantly bluer, two eccentric planets [a third eccentric planet, HAT-P-2b ([3.6]−[4.5] = 0), is compatible with the colourless L sequence].
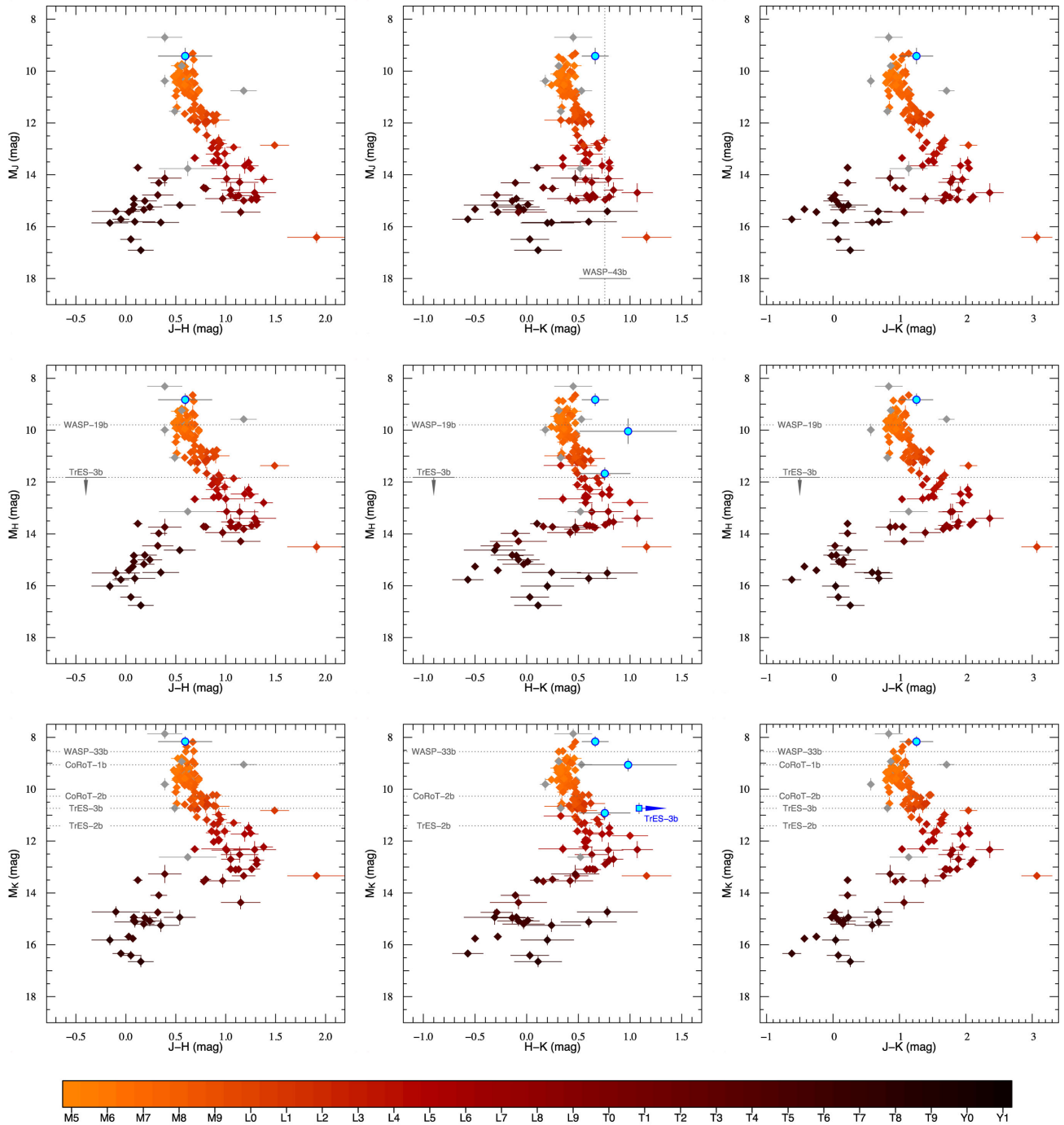
Figure 3. Near-infrared colour–magnitude diagrams, using the 2MASS photometric system (i.e. the *J*, *H* and *K*$_S$ bands). The blue dots show the dayside emission of transiting planets observed during occultation. Squares and arrows represent upper limits. Lines labelled with the name of a planet show the position of systems where colour or absolute magnitude is missing (not all cases are represented, for clarity). The coloured diamonds underlying the plots are brown dwarfs and directly imaged planets, whose magnitudes are listed in Dupuy & Liu (2012). Colours represent the spectral class of the object, spanning from M5 (orange) to Y1 (black). Unclassified objects are in grey.

The scatter in colour increases for increasing magnitudes: objects brighter than the median magnitude (GJ 436b removed) consistently have an rms in colour lower than objects fainter than the median magnitude. This is not because intrinsically fainter planets produce weaker (and harder to measure) occultations. Some of the most significant detections [for instance HD 189733Ab ($M_{[3.6]} = 11.1$, $[3.6]−[4.5] = 0.1$), HD 209458b ($M_{[3.6]} = 10.4$, $[3.6]−[4.5] = 0.8$)] are amongst the fainter planets. The graphs shuffled borderline and

significant measurements by using absolute magnitudes. A clear detection arises because the host star and the planet are bright in apparent magnitudes, for instance thanks to their proximity to the Solar system.

The known hot Jupiters' diversity in radius ($0.8–2R_{\rm Jup}$), which does not exist for field brown dwarfs, cannot be held responsible for the scatter either. A change in radius translates with a decrease in absolute magnitude, but no change in colour as shown in Fig. 6;
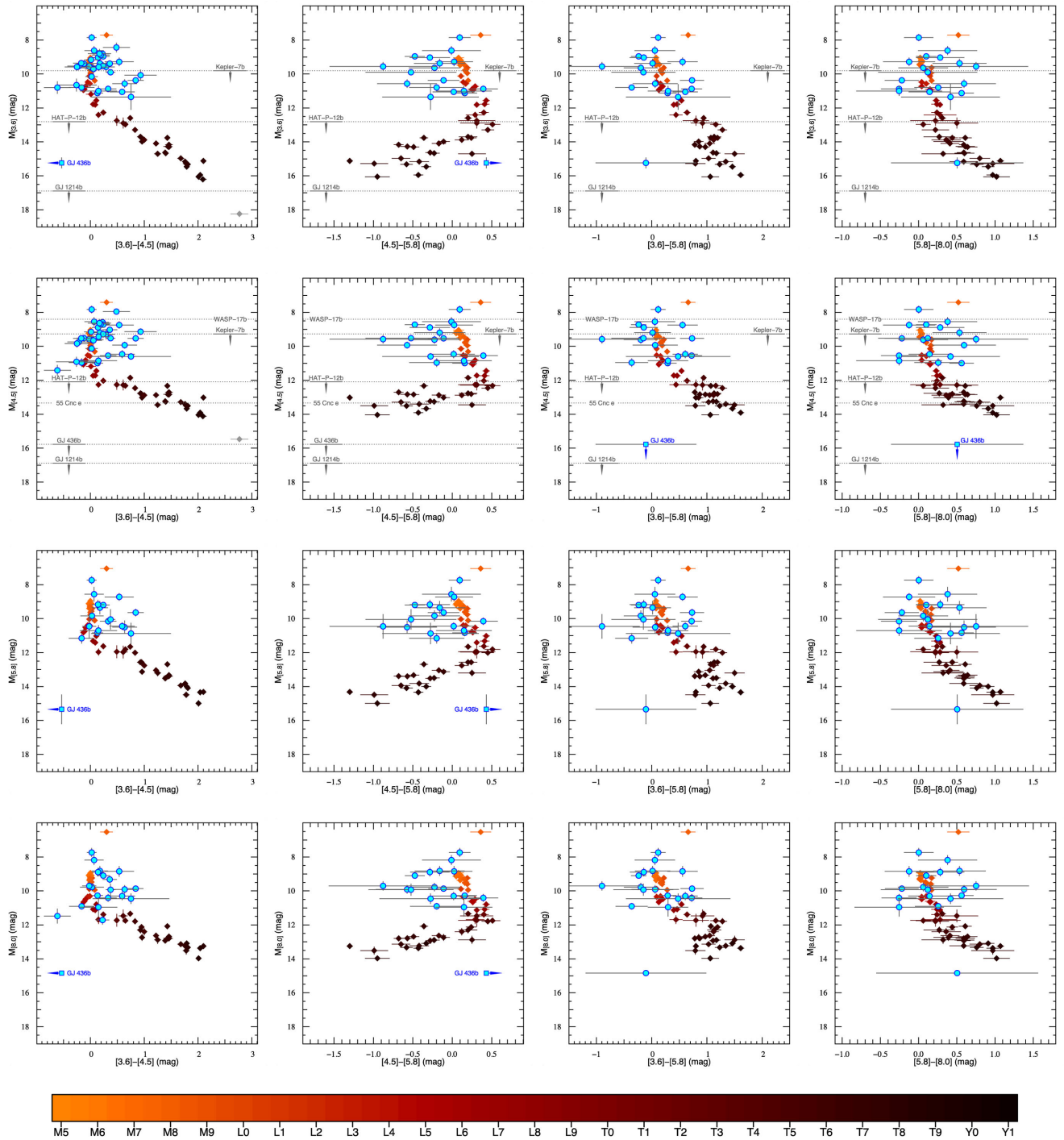
Figure 4. Mid-infrared colour–magnitude diagrams, using *Spitzer*'s IRAC photometric system. The blue dots show the dayside emission of transiting planets observed during occultation. Squares and arrows represent upper limits. Lines labelled with the name of a planet show the position of systems where colour or absolute magnitude is missing (not all cases are represented, for clarity). The coloured diamonds underlying the plots are ultra-cool dwarfs and directly imaged planets, whose magnitudes are listed in Dupuy & Liu (2012). Colours represent the spectral class of the object, spanning from M5 (orange) to Y1 (black). The only unclassified object here, in grey, is WD 0806-661B (Luhman et al. 2012).

when we compare with blackbodies, the current effects are much larger. This forces us to turn to other processes such as an increased diversity (in atmospheric structure or in absorbents) at colder temperatures, or to some intrinsic variability (with an amplitude ∼1.5 mag). If such is the case, repeated measurements should be attempted.

3.3.2 [4.5]−[5.8]

Brown dwarfs face a similar pattern as in the previous subsection, but orientated in the opposite direction. It also marks the transition between the L and T spectral classes. With decreasing temperatures, CO (that has absorption in the IRAC 2 bandpass) reacts with

H_2 to produce CH_4; it also produces H_2O that has several important absorption features around 5.8 μm. This makes the atmosphere become increasingly bluer with decreasing effective temperature.

The hot Jupiters, again, are all located in the absolute magnitude range of the M and L sequence. Apart from GJ 436b, all are marginally bluer than their ultra-cool dwarf counterparts. Would we consider each planet individually, we would conclude that each is consistent with the M and L sequence when in fact the general population clearly is not. It is systematically biased towards the blue. They have a mean colour inferior to 0 when all brown dwarfs are above 0 in the same absolute magnitude range. Water absorption has been noticed in several transmitted spectra (e.g. Deming et al. 2013), which would indicate that planets may depart from ultra-cool dwarfs' atmospheres in that water absorption appears at higher temperatures.

Alternatively, planetary atmospheres and ultra-cool dwarfs could be reconciled if ultra-cool dwarfs contain an absorbant around 4.5 μm that planets do not possess. If present, it would increase the planets' absolute magnitudes in the IRAC 2 channel at 4.5 μm, moving each point closer to 0.

3.3.3 [3.6]−[5.8] and [5.8]−[8.0]

Those two colours show a redward trend with decreasing luminosity. At [3.6]−[5.8] and at [5.8]−[8.0], planets and ultra-cool dwarf overlap very well: as many objects are found on either side of the brown dwarf sequence showing statistical agreement. Planets may be slightly offset towards redder colours, in [5.8]−[8.0] but only marginally so at the moment.

This agreement between planets and ultra-cool dwarfs could in principle act as a sort of calibration, validating that measurements in those bands are well estimated (in value and error bar). However, we have to remember here that hot Jupiters are significantly larger than the typical brown dwarf ($\sim$ 1.3–1.6R_{Jup} versus 0.8–0.9R_{Jup}). Reducing the planet size to the brown dwarf level should normally lead the planets to be dimmer by 0.8–1.5 mag (see Fig. 6 and Section 4). At first sights, both classes of objects should not be compatible. The fact that both groups have similar absolute magnitudes indicates that hot Jupiters have lower surface emissivity than ultra-cool dwarfs.

3.3.4 Summary from mid-IR colours

If a reason is found to explain the apparent agreement at [3.6]−[5.8] and [5.8]−[8.0], then we could conclude that the 4.5 μm band measurements are at the source of the observed divergence between irradiated gas giants and brown dwarfs in the [3.6]−[4.5] and [4.5]−[5.8] colours. Introducing some additional absorber within the planets' spectrum, around 4.5 μm, would move planets closer to 0 in both diagrams while keeping the [3.6]−[5.8] and [5.8]−[8.0] untouched. The fact that the intrinsically fainter planets display a greater divergence from the ultra-cool dwarfs in colours based on the 4.5 μm band may imply that they have an increased atmospheric diversity, some of them with, and some without, that absorbant. We prefer this interpretation over intrinsic variability whose otherwise required amplitude would seem too large to explain the data. The discrepant [4.5] band has been noticed by a number of authors, with Knutson et al. (2009) proposing that a temperature inversion in the temperature–pressure profile is responsible (Fortney et al. 2008). However, this interpretation has been disputed by Madhusudhan et al. (2011), who argue that disparities in relative abundances, notably the carbon-to-oxygen ratio, can reproduce the observations equally well.

A number of other measurements exist, notably observed in narrow bands (Gillon et al. 2009, 2012; Smith et al. 2011; Crossfield et al. 2012; Anderson et al. 2013; Lendl et al. 2013), in the z' band (López-Morales et al. 2010; Abe et al. 2013; Lendl et al. 2013) or observed by folding the *CoRoT* and *Kepler* light curves (e.g. Alonso et al. 2009; Snellen, de Mooij & Albrecht 2009; Demory et al. 2013; Morris, Mandell & Deming 2013; Sanchis-Ojeda et al. 2013). Because of a lack of measured brown dwarfs to compare them to and often because of a lack of apparent magnitudes in those particular bands, it seemed futile to do this exercise at this time. It will however become something worth investigating.

4 COMPARISON WITH BLACKBODIES

Hot Jupiter emission measurements are often compared to complex models and to blackbodies, with frequent claims that planet spectra are compatible with the shape expected of a blackbody. WASP-12Ab is one of the most noticeable examples (Crossfield et al. 2012). Hansen, Schwartz & Cowan (2014) surveyed the literature for objects whose emission has been detected in several data sets at the same wavelength and, taking the variation in results as a systematic error bar, found that planets have featureless spectra resembling blackbodies.

To answer this claim, and also because we should not expect irradiated planets and ultra-cool dwarfs to be exactly the same, plotting the location of blackbodies within a colour–magnitude diagram seemed warranted. The blackbody loci can provide context by revealing how brown dwarfs depart from a blackbody and how irradiated gas giants compare to these departures. Figs 5 and 6 have a 0.9R_{Jup}- and a 1.8R_{Jup}-sized blackbody plotted for all temperatures between 4000 and 400 K. Those sizes were chosen as they represent the maximum size brown dwarfs are expected to have (with an age >1 Gyr; Baraffe et al. 2003), and the approximate size of WASP-12Ab, one of the largest known exoplanet.

If planets were blackbodies, their measurements should be comprised strictly between the 0.9 and 1.8R_{Jup} blackbodies. They cannot be above and cannot be below that strip (except for HD 149026b and GJ 436b). In the near-infrared (the only transiting planet in Fig. 5) and mid-infrared, WASP-12Ab is lying near or on top of the expected blackbody line, in absolute magnitude and colour. Its location is also slightly above the 3000 K mark, which is compatible with its estimated equilibrium temperature of 2990 ± 110 K as provided by Crossfield et al. (2012).

Whether WASP-12Ab follows the behaviour of a late M dwarf better than a blackbody is irrelevant in this case: in all colours, the M and L sequence intersects with the expected blackbody line at WASP-12Ab's location in the colour–magnitude diagram.[3] The planet is where it ought to be. Having only few examples to work with, we added to Fig. 5 the directly imaged planets (Table B1). Apart from the recently announced GU Psc b (Naud et al. 2014), those young planets show good agreement with their M- and L-dwarf counterparts, but continue to be redder and fainter instead of turning into the blueward L–T transition, not unlike grey atmospheres. Irradiated planets could follow blackbodies, the ultra-cool dwarf's sequence, the path of the young directly imaged planets, or their own sequence. To differentiate between these four solutions, measurements of cooler transiting planets are required

---

[3] Reflected light likely plays no part in placing WASP-12Ab at this special location. It is expected to be about three orders of magnitude fainter than thermal emission (Seager & Deming 2010).
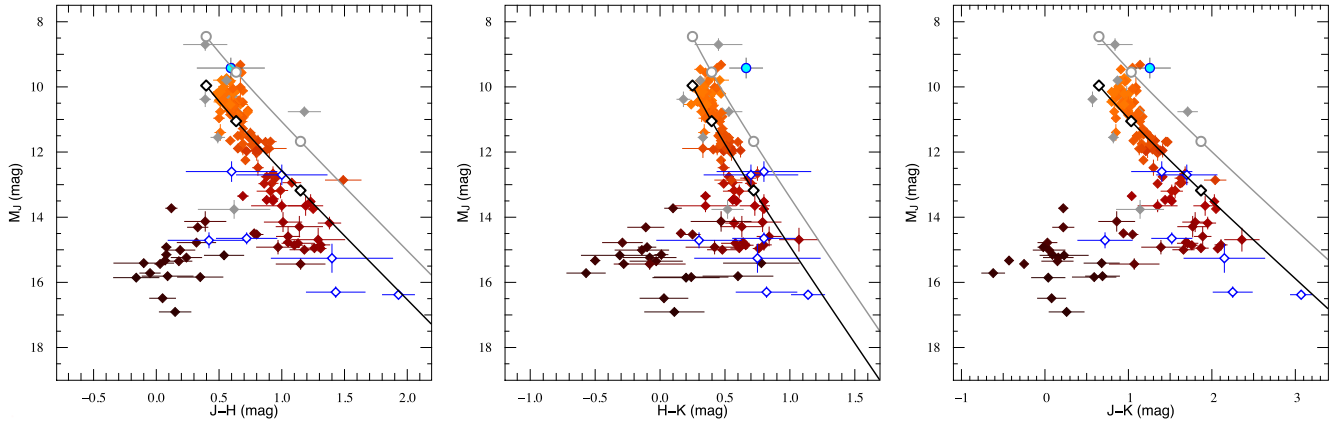
Figure 5. Same diagrams as the top line in Fig. 3 but showcasing the behaviour of blackbodies at 10 pc, whose effective temperature is changed while keeping its size constant. The plain black line is for a $0.9R_{Jup}$ object, similar to the radius of a brown dwarf, and the plain grey line represents a $1.8R_{Jup}$, the size of WASP-12Ab. The white filled diamonds ($0.9R_{Jup}$) and dots ($1.8R_{Jup}$) along the blackbodies indicate the location of a 4000, 3000 and 2000 K object. For reference, the blue, empty diamonds highlight the position of young, directly detected exoplanets whose data are given in Table B1.
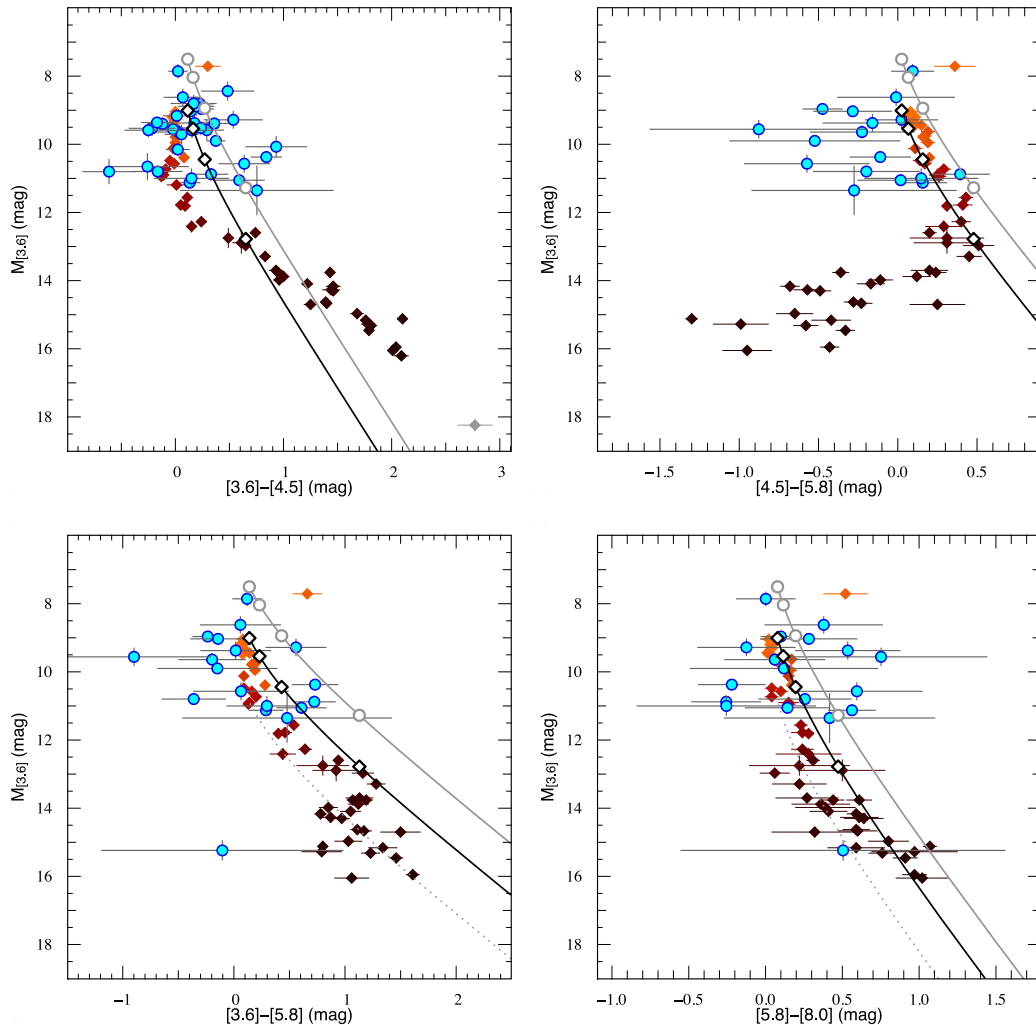
Figure 6. Same diagrams as the top line in Fig. 4 but showcasing the behaviour of blackbodies at 10 pc whose effective temperature is changed while keeping its size constant. In plain black, is drawn a $0.9R_{Jup}$ object, similar to the radius of a brown dwarf, and in plain grey a $1.8R_{Jup}$, the size of WASP-12Ab. The two bottom panels have an added dotted grey line, which is a blackbody with the size of GJ 436b ($0.38R_{Jup}$). The marks along the blackbodies indicate the expected location of a 4000, 3000, 2000 and 1000 K object.

in near-infrared bands. HAT-P-12b and WASP-80b are good contenders.

In the mid-infrared, the picture is more complex. In the $M_{[3.6]}$ versus [3.6]−[4.5] diagram, there are seven planets redder or brighter than the 1.8$R_{\rm Jup}$ blackbody. 13 systems are bluer or fainter than the 0.9$R_{\rm Jup}$ blackbody. Due to the dispersion (increasing with increasing magnitude), neither the brown dwarfs nor the blackbodies would seem to better explain all the measurements. We note that only two systems are more than 1σ above the 1.8$R_{\rm Jup}$ blackbody (HD 209458b and XO-4b), and one (WASP-8Ab) is away from the brown dwarfs. All other gas giants lie in agreement with a triangular confinement bordered by the blackbody on one side and the ultra-cool dwarf atmospheres on the other two. Targeting planets at the cool junction between the T dwarfs and the blackbody expectations will show if planets follow the T sequence, a blackbody, or their own sequence (for example when reflected starlight starts producing a strong effect). This means studying gas giants cooler than 1000 K (whose size would presumably be closer to 0.9 than 1.8$R_{\rm Jup}$).

The $M_{[3.6]}$ versus [4.5]−[5.8] diagram shows that the L sequence is slightly brighter than a 0.9$R_{\rm Jup}$ blackbody would predict, but generally follows the same slope. Brown dwarfs clearly depart when they transition to the T spectral class. In Section 3.3.2, we noted the blueward bias of hot Jupiters. This is strengthened when compared to a blackbody. Planets clearly depart. If each measurement is only 1σ–2σ away, what we lack in precision we gain in the number of systems measured. Hot Jupiters are not featureless. Again here, the departure between the brown dwarfs and the blackbody happens below 1000 K.

Gas giants and ultra-cool dwarfs agree well in $M_{[3.6]}$ versus [3.6]−[5.8]. However, planets do not match the expectations of a blackbody: All but four planets are found bluer or fainter than the 0.9$R_{\rm Jup}$ blackbody line. The fact that planets follow the same slope as a blackbody suggests a behaviour similar to a grey atmosphere, implying that opacities in these bands are grey. Hot Jupiters are not blackbodies and here behave more like dwarfs do. The final diagram, plotting $M_{[3.6]}$ versus [5.8]−[8.0], shows good agreement: brown dwarfs appear to follow the expected blackbody (being slightly below, maybe evidence they are slightly smaller than 0.9$R_{\rm Jup}$), so do hot Jupiters but with a large scatter. This would indicate that the opacity is grey in these bands and approaches the Planck law.

The location of a blackbody with the size of GJ 436b (0.38$R_{\rm Jup}$) was added and goes right through its measurement at [5.8]−[8.0]. A change in radius is only a translation in absolute magnitude. GJ 436b sits right at the 1000 K marks, which would imply a similar temperature, much higher than its estimated equilibrium temperature of ~700 K (Deming et al. 2007). If this is not the indication of excess energy produced by its ongoing tidal circularisation (Maness et al. 2007; Beust et al. 2012), this should be seen as a reminder that effective temperature is different from equilibrium temperature and that touching the blackbody sequence does not mean a measurement agrees with it, as temperature too needs to be accounted for. Shape is not all.

5 DISCUSSION AND CONCLUSION

We computed photometric distances that allowed us to obtain the absolute magnitude of occulting planets. They were used to compile colour–magnitude diagrams. Planets on their own would not offer much information. This is why we compared their location in these diagrams to the location of very low mass stars and field brown dwarfs, and to the behaviour expected of pure blackbodies. By

defining a blackbody sequence with a lower size of 0.9$R_{\rm Jup}$ and an upper one of 1.8$R_{\rm Jup}$, we describe a locus in the form of a strip where all hot Jupiters should congregate would they follow the Planck law.

In the near-infrared, three clear conclusions can be drawn.

(i) Planets are brighter in $K_{\rm S}$-band measurements, and in average redder than the M and L brown dwarf sequence (this probably has an instrumental origin).

(ii) WASP-12Ab is as much compatible with a blackbody as with the M and L sequences, because that is the location where both intersect.

(iii) A clear distinction between irradiated gas giants following a brown dwarf behaviour, the young directly imaged planets or a blackbody will emerge for equilibrium temperatures cooler than ~2000 K.

In the mid-infrared, we obtained the following general trends.

(i) Gas giants are only in agreement with the blackbody locus in the [5.8]−[8.0] colour. Deviations, made significant by the number of objects considered, in the other colours imply that planets are not pure blackbodies, although individual objects may appear to be.

(ii) Gas giants are bluer in the [4.5]−[5.8] colour than a blackbody or the M and L brown dwarf sequence. This shows that hot Jupiters are not featureless.

(iii) Combining this with an increased scatter as magnitudes increase in the [3.6]−[4.5] provides support that some gas giants are lacking an absorbant at 4.5 μm.

(iv) This affects only certain planets making us conclude that atmospheric diversity increases with decreasing absolute magnitude, presumably, with decreasing equilibrium temperature.

(v) Clearly associating planets to the brown dwarf locus or to the blackbody strip can be made by obtaining the emission (dayside or nightside) of gas giants with effective temperatures below 1000 K at [3.6] and [4.5].

It is worth noting at this point that the observed increase in atmospheric diversity is found under the upper limits placed by Demory et al. (2013) on Kepler-7b. This planet's detected occultation and phase curve in the *Kepler* bandpass have been interpreted as reflected light from an inhomogeneous, high albedo, cloud layer, mostly located on the dayside. From studying HD 189733Ab's phase curve inside a colour–magnitude diagram, Triaud (2014) made a similar inference: the presence of clouds can hide the effect of some absorbing species or can locally change the atmospheric chemistry. We can therefore wonder whether the existence of clouds can be linked to the presence or absence of an absorbing feature in *Spitzer*'s 4.5 μm channel that leads to the scatter present in the [3.6]−[4.5] and [4.5]−[5.8] colours.

If brown dwarf atmospheres and irradiated exoplanets are set to coincide, then it is perhaps not surprising that since most exoplanets fall in the range occupied by the M and L types, they too would have an opaque cloud layer at least on the dayside. Clouds are likely to leak over the terminator covering transmitted features. This provides context to the frequently announced featureless transmission spectra on several exoplanets (e.g. Bean, Miller-Ricci Kempton & Homeier 2010; Berta et al. 2012; Jordán et al. 2013; Sing et al. 2013). GJ 436b is found on the continuation of the M and L sequences, and also shows a featureless transmission spectrum (Knutson et al. 2014). The scatter in colour of the emitted spectra for the colder of the transiting gas giants can give hope that some will possess an inhomogeneous cloud cover, revealing the deeper parts of their atmospheres through cloud holes. Using colour–magnitude diagrams would become a useful tool to select the right exoplanet

sample before attempting an observing campaign aimed at producing transmission spectra.

Burrows & Ostriker (2014) point out, in their supplementary materials, that for an equivalent emerging flux, the spectra of an irradiated and of an isolated planet are dissimilar, notably by possessing widely different temperature–pressure profiles. The widening range in colour could also originate from distinctions in the impacting irradiative stellar flux, or on how this energy affects different atmospheres. An irradiated planet, for instance, emits more strongly at 4.5 μm than its isolated equivalent.

An obvious extension of this work would be to explore other colours, notably in some narrow bands where successful occultation measurements have been obtained by a number of investigators. Ultra-cool dwarf magnitudes can be obtained from the many spectra that have been acquired of these objects and integrating over the correct bandpasses. It would be interesting to know whether those fall into regions sensitive to additional species, which could greatly help our understanding of exoplanetary atmospheres. For instance, Demory et al. (2013) have shown how bright Kepler-7 is in *Kepler*'s optical bandpass, Kmag, compared to its mid-infrared magnitude. It is therefore likely that a Kmag-[3.6] or a Kmag-[4.5] would be a tracer of cloudy structures on the dayside of exoplanets. We cannot but encourage authors to report apparent magnitudes in the bands that they report occultations in.

From studying those diagrams, we can make judgements about the most interesting planets to obtain emission measurements on. Some objects are particular in deviating from the global trends we outlined above, with the clearest example found with GJ 436b. Its small size is not sufficient to explain its discrepancy. The absence of a detection in the 4.5 μm band signifies that it is the bluest object in the current sample in the [3.6]−[4.5] colour and the reddest in [4.5]−[5.8]. While being broadly consistent with the shape of a blackbody, its inferred effective temperature ($\sim$1000 K) appears unreasonably high. The study of the other smaller planets, GJ 1214 b (Charbonneau et al. 2009), GJ 3470 b (Bonfils et al. 2012) and HD 97658b (Dragomir et al. 2013), can show if they manifest an atmospheric behaviour similar to GJ 436b's.

Arguably there are now enough measurements over the M and L sequences; it is scientifically interesting to reserve our resources to extend beyond that range. Going further up along the M sequence would need hot Jupiters orbiting A stars (like WASP-33; Collier Cameron et al. 2010; Deming et al. 2012) that are hard to come about and hard to analyse: many A stars are within the instability strip and display oscillations (WASP-33 is a δ Scuti). Exploring further down, closer to the T regime, especially for equilibrium temperatures below 1000 K, can be achieved by targeting longer period planets (WASP-8Ab for example is close to the L–T transition; Queloz et al. 2010; Cubillos et al. 2013). The main issue in observing colder planets is the weak signals that can be expected from them. This can be mitigated by selecting host stars of late spectral classes such as WASP-80 (Triaud et al. 2013b).

So far very few transiting (or occulting) brown dwarfs have been detected (Deleuil et al. 2008; Anderson et al. 2011b; Bouchy et al. 2011; Siverd et al. 2012; Díaz et al. 2013). Because they often orbit hot and large stars, their occultations are weak. Beatty et al. (2014) however managed to measure KELT-1b. However, those brown dwarfs are mostly found on short orbits, like hot Jupiters. They have inferred temperatures similar to M or L objects but differ from usual brown dwarfs in that they are inflated. Because of their size, they fall on isochrones younger than the inferred age of the star they orbit (Triaud et al. 2013a). Proximity acts like a rejuvenation. Obtaining several brightness measurements over the M, L and T

range, preferably on long-period objects, would in principle procure a radius calibration for field brown dwarfs.

REFERENCES

Abe L. et al., 2013, A&A, 553, A49
Ackerman A. S., Marley M. S., 2001, ApJ, 556, 872
Alonso R. et al., 2004, ApJ, 613, L153
Alonso R. et al., 2008, A&A, 482, L21
Alonso R., Guillot T., Mazeh T., Aigrain S., Alapini A., Barge P., Hatzes A., Pont F., 2009, A&A, 501, L23
Alonso R., Deeg H. J., Kabath P., Rabus M., 2010, AJ, 139, 1481
Anderson D. R. et al., 2008, MNRAS, 387, L4
Anderson D. R. et al., 2010, ApJ, 709, 159
Anderson D. R. et al., 2011a, MNRAS, 416, 2108
Anderson D. R. et al., 2011b, ApJ, 726, L19
Anderson D. R. et al., 2013, MNRAS, 430, 3422
Anglada-Escudé G., Rojas-Ayala B., Boss A. P., Weinberger A. J., Lloyd J. P., 2013, A&A, 551, A48
Artigau É., Bouchard S., Doyon R., Lafrenière D., 2009, ApJ, 701, 1534
Bakos G. Á. et al., 2007a, ApJ, 656, 552
Bakos G. Á. et al., 2007b, ApJ, 670, 826
Bakos G. Á. et al., 2011, ApJ, 742, 116
Baraffe I., Chabrier G., Allard F., Hauschildt P. H., 1998, A&A, 337, 403
Baraffe I., Chabrier G., Barman T. S., Allard F., Hauschildt P. H., 2003, A&A, 402, 701
Barge P. et al., 2008, A&A, 482, L17

Baskin N. J. et al., 2013, ApJ, 773, 124
Bean J. L., Miller-Ricci Kempton E., Homeier D., 2010, Nature, 468, 669
Bean J. L., Désert J.-M., Seifahrt A., Madhusudhan N., Chilingarian I., Homeier D., Szentgyorgyi A., 2013, ApJ, 771, 108
Beatty T. G. et al., 2014, ApJ, 783, 112
Beerer I. M. et al., 2011, ApJ, 727, 23
Berta Z. K. et al., 2012, ApJ, 747, 35
Beust H., Bonfils X., Montagnier G., Delfosse X., Forveille T., 2012, A&A, 545, A88
Blecic J. et al., 2013, ApJ, 779, 5
Blecic J. et al., 2014, ApJ, 781, 116
Bonfils X. et al., 2012, A&A, 546, A27
Bonnefoy M. et al., 2011, A&A, 528, L15
Bonnefoy M. et al., 2013, A&A, 555, A107
Bouchy F. et al., 2005, A&A, 444, L15
Bouchy F. et al., 2011, A&A, 525, A68
Burgasser A. J., Marley M. S., Ackerman A. S., Saumon D., Lodders K., Dahn C. C., Harris H. C., Kirkpatrick J. D., 2002, ApJ, 571, L151
Burke C. J. et al., 2007, ApJ, 671, 2115
Burrows A. S., Ostriker J. P., 2014, Proc. Natl. Acad. Sci., 111, 2409
Butler R. P., Vogt S. S., Marcy G. W., Fischer D. A., Wright J. T., Henry G. W., Laughlin G., Lissauer J. J., 2004, ApJ, 617, 580
Caballero J. A. et al., 2007, A&A, 470, 903
Cáceres C. et al., 2011, A&A, 530, A5
Carson J. et al., 2013, ApJ, 763, L32
Charbonneau D., Brown T. M., Latham D. W., Mayor M., 2000, ApJ, 529, L45
Charbonneau D. et al., 2005, ApJ, 626, 523
Charbonneau D. et al., 2009, Nature, 462, 891
Chauvin G., Lagrange A.-M., Dumas C., Zuckerman B., Mouillet D., Song I., Beuzit J.-L., Lowrance P., 2004, A&A, 425, L29
Christiansen J. L. et al., 2010, ApJ, 710, 97
Collier Cameron A. et al., 2007, MNRAS, 375, 951
Collier Cameron A. et al., 2010, MNRAS, 407, 507
Cox A. N., 2000, Allen's Astrophysical Quantities. AIP Press, New York
Croll B., Albert L., Lafreniere D., Jayawardhana R., Fortney J. J., 2010a, ApJ, 717, 1084
Croll B., Jayawardhana R., Fortney J. J., Lafrenière D., Albert L., 2010b, ApJ, 718, 920
Crossfield I. J. M., Barman T., Hansen B. M. S., Tanaka I., Kodama T., 2012, ApJ, 760, 140
Crossfield I. J. M. et al., 2014, Nature, 505, 654
Cubillos P. et al., 2013, ApJ, 768, 42
Cushing M. C. et al., 2011, ApJ, 743, 50
Cutri R. M. et al., 2003, VizieR Online Data Catalog, 2246, 0
Cutri R. M. et al., 2012, VizieR Online Data Catalog, 2311, 0
Dawson R. I., Fabrycky D. C., 2010, ApJ, 722, 937
de Mooij E. J. W., de Kok R. J., Nefs S. V., Snellen I. A. G., 2011, A&A, 528, A49
de Mooij E. J. W., Brogi M., de Kok R. J., Snellen I. A. G., Kenworthy M. A., Karjalainen R., 2013, A&A, 550, A54
Deleuil M. et al., 2008, A&A, 491, 889
Delorme P. et al., 2013, A&A, 553, L5
Deming D., Harrington J., Laughlin G., Seager S., Navarro S. B., Bowman W. C., Horning K., 2007, ApJ, 667, L199
Deming D. et al., 2011, ApJ, 726, 95
Deming D. et al., 2012, ApJ, 754, 106
Deming D. et al., 2013, ApJ, 774, 95
Demory B.-O., Seager S., 2011, ApJS, 197, 12
Demory B.-O. et al., 2011, A&A, 533, A114
Demory B.-O., Gillon M., Seager S., Benneke B., Deming D., Jackson B., 2012, ApJ, 751, L28
Demory B.-O. et al., 2013, ApJ, 776, L25
Díaz R. F. et al., 2013, A&A, 551, L9
Dragomir D. et al., 2013, ApJ, 772, L2
Droege T. F., Richmond M. W., Sallman M. P., Creager R. P., 2006, PASP, 118, 1666
Dupuy T. J., Liu M. C., 2012, ApJS, 201, 19

Enoch B. et al., 2011, AJ, 142, 86
Flower P. J., 1996, ApJ, 469, 355
Fortney J. J., Lodders K., Marley M. S., Freedman R. S., 2008, ApJ, 678, 1419
Fressin F., Knutson H. A., Charbonneau D., O'Donovan F. T., Burrows A., Deming D., Mandushev G., Spiegel D., 2010, ApJ, 711, 374
Gillon M., Pont F., Moutou C., Bouchy F., Courbin F., Sohy S., Magain P., 2006, A&A, 459, 249
Gillon M. et al., 2007, A&A, 472, L13
Gillon M. et al., 2009, A&A, 506, 359
Gillon M. et al., 2010, A&A, 511, A3
Gillon M. et al., 2012, A&A, 542, A4
Gillon M., Triaud A. H. M. J., Jehin E., Delrez L., Opitom C., Magain P., Lendl M., Queloz D., 2013, A&A, 555, L5
Gillon M. et al., 2014, A&A, 563, A21
Hansen C. J., Schwartz J. C., Cowan N. B., 2014, preprint (arXiv:1402.6699)
Hartman J. D. et al., 2009, ApJ, 706, 785
Hebb L. et al., 2009, ApJ, 693, 1920
Hebb L. et al., 2010, ApJ, 708, 224
Heinze A. N. et al., 2013, ApJ, 767, 173
Hellier C. et al., 2009, Nature, 460, 1098
Hellier C. et al., 2011, A&A, 535, L7
Henry G. W., Marcy G. W., Butler R. P., Vogt S. S., 2000, ApJ, 529, L41
Hertzsprung E., 1911, Publ. Astrophys. Obs. Potsdam, 22, No. 63
Høg E. et al., 2000, A&A, 355, L27
Johns-Krull C. M. et al., 2008, ApJ, 677, 657
Jordán A. et al., 2013, ApJ, 778, 184
Joshi Y. C. et al., 2009, MNRAS, 392, 1532
Kirkpatrick J. D., 2005, ARA&A, 43, 195
Kirkpatrick J. D. et al., 2011, ApJS, 197, 19
Knapp G. R. et al., 2004, AJ, 127, 3553
Knutson H. A., Charbonneau D., Allen L. E., Burrows A., Megeath S. T., 2008, ApJ, 673, 526
Knutson H. A., Charbonneau D., Burrows A., O'Donovan F. T., Mandushev G., 2009, ApJ, 691, 866
Knutson H. A. et al., 2012, ApJ, 754, 22
Knutson H. A., Benneke B., Deming D., Homeier D., 2014, Nature, 505, 66
Kovács G. et al., 2007, ApJ, 670, L41
Lagrange A.-M. et al., 2009, A&A, 493, L21
Latham D. W., Stefanik R. P., Mazeh T., Mayor M., Burki G., 1989, Nature, 339, 38
Latham D. W. et al., 2009, ApJ, 704, 1107
Latham D. W. et al., 2010, ApJ, 713, L140
Laughlin G., Deming D., Langton J., Kasen D., Vogt S., Butler P., Rivera E., Meschiari S., 2009, Nature, 457, 562
Lendl M., Gillon M., Queloz D., Alonso R., Fumel A., Jehin E., Naef D., 2013, A&A, 552, A2
Lewis N. K. et al., 2013, ApJ, 766, 95
López-Morales M., Coughlin J. L., Sing D. K., Burrows A., Apai D., Rogers J. C., Spiegel D. S., Adams E. R., 2010, ApJ, 716, L36
Luhman K. L., Burgasser A. J., Labbé I., Saumon D., Marley M. S., Bochanski J. J., Monson A. J., Persson S. E., 2012, ApJ, 744, 135
Machalek P., McCullough P. R., Burke C. J., Valenti J. A., Burrows A., Hora J. L., 2008, ApJ, 684, 1427
Machalek P., McCullough P. R., Burrows A., Burke C. J., Hora J. L., Johns-Krull C. M., 2009, ApJ, 701, 514
Machalek P., Greene T., McCullough P. R., Burrows A., Burke C. J., Hora J. L., Johns-Krull C. M., Deming D. L., 2010, ApJ, 711, 111
Madhusudhan N., Mousis O., Johnson T. V., Lunine J. I., 2011, ApJ, 743, 191
Magain P., Courbin F., Sohy S., 1998, ApJ, 494, 472
Mahtani D. P. et al., 2013, MNRAS, 432, 693
Mancini L. et al., 2014, A&A, 562, A126
Mandushev G. et al., 2007, ApJ, 667, L195
Maness H. L., Marcy G. W., Ford E. B., Hauschildt P. H., Shreve A. T., Basri G. B., Butler R. P., Vogt S. S., 2007, PASP, 119, 90
Marley M. S., Seager S., Saumon D., Lodders K., Ackerman A. S., Freedman R. S., Fan X., 2002, ApJ, 568, 335

Marois C., Macintosh B., Barman T., Zuckerman B., Song I., Patience J., Lafrenière D., Doyon R., 2008, Science, 322, 1348

Maxted P. F. L., Koen C., Smalley B., 2011, MNRAS, 418, 1039

Maxted P. F. L. et al., 2013, MNRAS, 428, 2645

Mazeh T. et al., 2000, ApJ, 532, L55

McArthur B. E. et al., 2004, ApJ, 614, L81

McCullough P. R. et al., 2006, ApJ, 648, 1228

McCullough P. R. et al., 2008, preprint (arXiv:0805.2921)

Mohanty S., Jayawardhana R., Huélamo N., Mamajek E., 2007, ApJ, 657, 1064

Morris B. M., Mandell A. M., Deming D., 2013, ApJ, 764, L22

Naef D. et al., 2001, A&A, 375, L27

Naud M.-E. et al., 2014, ApJ, 787, 5

Noyes R. W. et al., 2008, ApJ, 673, L79

Nymeyer S. et al., 2011, ApJ, 742, 35

O'Donovan F. T. et al., 2006, ApJ, 651, L61

O'Donovan F. T. et al., 2007, ApJ, 663, L37

O'Donovan F. T., Charbonneau D., Harrington J., Madhusudhan N., Seager S., Deming D., Knutson H. A., 2010, ApJ, 710, 1551

O'Rourke J. G. et al., 2014, ApJ, 781, 109

Pál A. et al., 2008, ApJ, 680, 1450

Patten B. M. et al., 2006, ApJ, 651, 502

Perryman M. A. C. et al., 2001, A&A, 369, 339

Pollacco D. et al., 2008, MNRAS, 385, 1576

Queloz D. et al., 2010, A&A, 517, L1

Radigan J., Jayawardhana R., Lafrenière D., Artigau É., Marley M., Saumon D., 2012, ApJ, 750, 105

Radigan J., Lafrenière D., Jayawardhana R., Artigau E., 2014, preprint (arXiv:1404.3247)

Reach W. T. et al., 2005, PASP, 117, 978

Rogers J. C., Apai D., López-Morales M., Sing D. K., Burrows A., 2009, ApJ, 707, 1707

Rogers J., López-Morales M., Apai D., Adams E., 2013, ApJ, 767, 64

Russell H. N., 1914a, Nature, 93, 227

Russell H. N., 1914b, Nature, 93, 252

Russell H. N., 1914c, Nature, 93, 281

Sahlmann J. et al., 2011, A&A, 525, A95

Sanchis-Ojeda R., Rappaport S., Winn J. N., Levine A., Kotson M. C., Latham D. W., Buchhave L. A., 2013, ApJ, 774, 54

Sato B. et al., 2005, ApJ, 633, 465

Schneider J., Dedieu C., Le Sidaner P., Savalle R., Zolotukhin I., 2011, A&A, 532, A79

Seager S., Deming D., 2010, ARA&A, 48, 631

Shannon C. E., 1949, Proc. IRE, 37, 10

Sing D. K. et al., 2013, MNRAS, 436, 2956

Siverd R. J. et al., 2012, ApJ, 761, 123

Smalley B. et al., 2010, A&A, 520, A56

Smith A. M. S., Anderson D. R., Skillen I., Collier Cameron A., Smalley B., 2011, MNRAS, 416, 2096

Smith A. M. S. et al., 2012, A&A, 545, A93

Snellen I. A. G., de Mooij E. J. W., Albrecht S., 2009, Nature, 459, 543

Southworth J., 2011, MNRAS, 417, 2166

Stetson P. B., 1987, PASP, 99, 191

Stevenson K. B. et al., 2012, ApJ, 754, 136

Street R. A. et al., 2010, ApJ, 720, 337

Todorov K., Deming D., Harrington J., Stevenson K. B., Bowman W. C., Nymeyer S., Fortney J. J., Bakos G. A., 2010, ApJ, 708, 498

Todorov K. O. et al., 2012, ApJ, 746, 111

Todorov K. O. et al., 2013, ApJ, 770, 102

Torres G. et al., 2007, ApJ, 666, L121

Torres G., Winn J. N., Holman M. J., 2008, ApJ, 677, 1324

Torres G., Andersen J., Giménez A., 2010, A&AR, 18, 67

Triaud A. H. M. J., 2014, MNRAS, 439, L61

Triaud A. H. M. J. et al., 2013a, A&A, 549, A18

Triaud A. H. M. J. et al., 2013b, A&A, 551, A80

Tsuji T., 2002, ApJ, 575, 264

van Leeuwen F., 2007, A&A, 474, 653

Wang W., van Boekel R., Madhusudhan N., Chen G., Zhao G., Henning T., 2013, ApJ, 770, 70

Wheatley P. J. et al., 2010, preprint (arXiv:1004.0836)

Wilson D. M. et al., 2008, ApJ, 675, L113

Wilson P. A., Rajan A., Patience J., 2014, A&A, 566, 111

Winn J. N. et al., 2011, ApJ, 737, L18

Wright J. T. et al., 2011, PASP, 123, 412

Zacharias N., Finch C. T., Girard T. M., Henden A., Bartlett J. L., Monet D. G., Zacharias M. I., 2013, AJ, 145, 44

Zhao M., Monnier J. D., Swain M. R., Barman T., Hinkley S., 2012a, ApJ, 744, 122

Zhao M., Milburn J., Barman T., Hinkley S., Swain M. R., Wright J., Monnier J. D., 2012b, ApJ, 748, L8

APPENDIX A: OBTAINING CALIBRATED APPARENT MAGNITUDES WITH *SPITZER*

Apparent magnitudes in all four IRAC bands are based on IRAC images calibrated by the standard *Spitzer* pipeline (version S18.18 or S18.25 depending on their availability at the time of the data reduction). They are delivered to the community as basic calibrated data (BCD) sets and can be easily found at the *Spitzer* Heritage Archive.[4] According to the brightness of each target, some sets were observed in the IRAC channels in sub-array mode, some in full-array mode and a number in both. This forced us to employ two different data reductions. The sub-array mode offers a high temporal resolution for observing very bright sources (available exposure times: 0.02, 0.1 and 0.4 s) on a portion of the array detector (32×32 pixels). The full-array mode provides 256×256 pixel ($5.22\,\mathrm{arcmin} \times 5.22\,\mathrm{arcmin}$) frames for longer exposure times of 2, 12, 30 and 100 s.

A1 Aperture photometry

Each BCD set provided by sub-array mode is composed of 64 sub-array images. These data are reduced according to the EXOPHOT PYRAF pipeline following Lanotte et al. (in preparation) to get raw light curves. For each sub-array image, a 2D elliptical Gaussian profile fit is performed on the point spread function (PSF) of the target to obtain its PSF centre coordinates. We operate aperture photometry thanks to the IRAF/DAOPHOT[5] software (Stetson 1987). For each sub-array image, the software measures the stellar flux on apertures centred on our estimated PSF locations, ranging from 2.5 to 5.9 pixels by increments of 0.1 pixel, and subtracts the background level evaluated in an annulus extending from 12 to 15 pixels from the centre of aperture. For each block of 64 sub-array images, the discrepant values for the measurements of the x- and y-position, and the stellar and background flux are rejected using a 3σ median clipping. The remaining measurements in each BCD set are averaged.

The full-array mode images are reduced in the same way, except that the PSF centres are determined by a flux-weighted centroid. This method is better adapted to lower signal-to-noise data.

At this stage, the first measurements of each light curve are discarded if they correspond to deviant values for all or some of the external parameters (detector or pointing stabilization). Finally, we perform for each light curve a moving median filtering to discard outlier measurements due, for instance, to cosmic hits. We also

---

[4] http://sha.ipac.caltech.edu/applications/Spitzer/SHA/

[5] IRAF is distributed by the National Optical Astronomy Observatory, which is operated by the Association of Universities for Research in Astronomy, Inc., under cooperative agreement with the National Science Foundation.

reject the measurements during a planetary transit, if present, to always consider the total stellar flux. Ideally one should measure the flux coming from the stellar system only during the occultation of the planet to only consider the stellar flux. However, the planetary emission is negligible in comparison to flux variations induced by instrumental effects such as the 'pixel-phase' and the 'ramp' effects. The first one lies in the dependence of the observed flux with the stellar centroid location on the pixel of the IRAC InSb (3.6 and 4.5 μm) arrays. It is due to the inhomogeneous intrapixel sensitivity combined to the jitter of the telescope and to the poor sampling of the PSF. The second effect is the increase of the detector response at the start of AORs and is attributed to a charge-trapping mechanism resulting in a dependence of the gain of the pixels to their illumination history. We refer the reader to Knutson et al. (2008) and references therein for more information about these instrumental systematics.

The pixel-phase response changed at the beginning of the *Warm* mission, with the consequence that the correction map of the cryogenic phase of *Spitzer* could not be used for all the data. Since no complete correction map is available for the *Warm* phase of *Spitzer* at the time of our analysis, we do not correct the flux measurements for the intra-pixel sensitivity. In practice, those intra-pixel flux variations are partially averaged out thanks to variations in the location of the PSF during an observational run. We do not model the 'ramp' effect but simply remove the more affected sequence of measurements.

For each data set (called AOR = Astronomical Observation Request in *Spitzer* terminology), we average all remaining measured stellar fluxes computed for each radius separately. We then apply the appropriate aperture correction to determine the stellar flux as it would be falling into a circular aperture radius of 10 pixels. This is carried out in order to remain consistent with the magnitude calibrations present in Reach et al. (2005). The IRAC instrument handbook provides aperture corrections for different aperture radii and background annuli. However, only three aperture corrections can be applied for the sub-array mode data, so that we generate other aperture correction factors to coincide with all our photometric apertures. Indeed, the accuracy of the flux measurement resides in the choice of the photometric aperture radius. While small aperture radii are dominated by imprecisions due to undersampling the PSF and pixel-to-pixel response, larger radii are affected by larger background contributions. We thus perform aperture photometry on deconvolved images reconvolved by the best-fitting partial PSF model to derive the aperture corrections required for deriving the observed flux of the star. The deconvolution photometry is made using DECPHOT following a procedure described in Gillon et al. (2006) and optimized for *Spitzer* data by Lanotte et al. (in preparation). DECPHOT is based on the image-deconvolution method of Magain, Courbin & Sohy (1998) that, contrarily to traditional deconvolution methods, respects the sampling theorem of Shannon (1949) and preserves the photometric flux. The aperture corrections are normalized to the flux falling into a circular aperture radius of 10 pixels subtracted to the background level measured in an annulus from 12 to 20 pixels.

Then we average all flux corrected for aperture and take the resulting value as the observed flux measurement for the data set. The mean of the errors on each corrected flux is taken as our error bar on the measured stellar flux. We convert the measured flux in jansky and apply the colour and inter-pixel corrections.[6] Finally, the

Table A1. Dilution factors in the stellar flux from CoRoT-2A and WASP-8A caused by their visual companion. These factors are estimated for a range of aperture radii.

| Aperture radius | Dilution (per cent) | | | |
| | CoRoT-2A | | WASP-8A | |
(pixels)	[3.6]	[4.5]	[3.6]	[4.5]
2.5	4.08	2.72	0.85	1.23
3.0	7.51	5.80	2.54	3.56
3.5	12.98	11.31	6.34	7.87
4.0	17.44	15.60	9.90	11.83
4.5	18.91	17.19	11.43	13.76

flux densities are converted into Vega apparent magnitudes using the zero-magnitude flux densities computed by Reach et al. (2005). The associated error bars are dominated by the uncertainty in the absolute calibration.

A2 Deconvolution of blended stars

Two systems in our sample (CoRoT-2 and WASP-8) are blended by a visual companion. Gillon et al. (2010) and Deming et al. (2011) have evaluated the dilution factor: the correction to the measured flux needed to remove the dilution caused by CoRotT-2A's visual companion. Their correction factors at 4.5 μm return a magnitude disparity of ∼0.3 mag using our measured fluxes using the method described above. No similar work has been done for WASP-8. In order to measure the dilution factor induced in the flux measurement with a higher precision, we performed once again a deconvolution of the data for those two stars. We used DECPHOT to operate aperture photometry on model images considering two stars or the target only. We compute the dilution factor for both systems using all our aperture radii to reduce the errors of the inferred factors. The standard deviations of CoRoT-2 and WASP-8 fluxes due to the change of aperture radius are 0.11 and 0.07 per cent, respectively, at 3.6 μm, and 0.04 and 0.08 per cent at 4.5 μm. For comparison, the standard deviations of isolated target fluxes due to the change of aperture radius are encompassed between 0.01 and 0.06 per cent. Table A1 gives dilution factors according to some aperture radius, the target and the instrument. With these factors, fluxes for each aperture are corrected, and the same procedure as described in the previous section is carried out to yield corrected apparent magnitudes.

APPENDIX B: TABLES

Table B1. Absolute magnitudes reported for some directly imaged planets.

Name	M_J	M_H	M_{K_s}	Refs
κ And b	12.7 ± 0.3	11.7 ± 0.2	11.0 ± 0.4	1
HR 8799 b	16.30 ± 0.16	14.87 ± 0.17	14.05 ± 0.08	2
HR 8799 c	14.65 ± 0.17	13.93 ± 0.17	13.13 ± 0.08	2
HR 8799 d	15.26 ± 0.43	13.86 ± 0.22	13.11 ± 0.12	2
2M 1207 b	16.38 ± 0.09	14.45 ± 0.09	13.31 ± 0.08	3, 4
β Pic b	12.6 ± 0.3	12.0 ± 0.2	11.2 ± 0.1	5, 6, 7
GU Psc b	14.71 ± 0.23	14.29 ± 0.23	13.99 ± 0.23	8

References: (1) Carson et al. (2013); (2) Marois et al. (2008); (3) Chauvin et al. (2004); (4) Mohanty et al. (2007); (5) Lagrange et al. (2009); (6) Bonnefoy et al. (2011); (7) Bonnefoy et al. (2013); (8) Naud et al. (2014).

---

[6] See sections 4.4 and 4.5 of the *Spitzer* Observer's Manual and http://irsa.ipac.caltech.edu/data/SPITZER/docs/irac/warmfeatures/

Table B2. Parallactic distances and apparent magnitudes from the literature, presented with photometric distances, obtained from absolute visual magnitudes M_V computed as described in the text, using the Vega-based magnitude convention.

Name	Parallactic distance (pc)	Photometric distance (pc)	Distance modulus $(m_V - M_V)$	Apparent magnitudes							Refs
				m_J	m_H	m_{K_S}	$m_{[3.6]}$	$m_{[4.5]}$	$m_{[5.8]}$	$m_{[8.0]}$	
HD 189733A	19.45 ± 0.26	19.1 ± 1.0	1.41 ± 0.12	6.073 ± 0.032	5.587 ± 0.031	5.541 ± 0.021	5.450 ± 0.065	5.530 ± 0.061	5.971 ± 0.063	5.968 ± 0.059	1,2,3,5
HD 209458	49.6 ± 2.0	49.0 ± 2.2	3.45 ± 0.10	6.591 ± 0.020	6.366 ± 0.038	6.308 ± 0.026	6.258 ± 0.043	6.305 ± 0.035	6.791 ± 0.064	6.765 ± 0.057	1,2,3,5
HD 80606	–	65.8 ± 3.9	4.09 ± 0.13	7.702 ± 0.030	7.400 ± 0.034	7.316 ± 0.020	7.257 ± 0.063	7.348 ± 0.037	–	7.742 ± 0.061	1,3,5
HD 149026	79.4 ± 4.4	80.8 ± 4.0	4.54 ± 0.11	7.118 ± 0.024	6.899 ± 0.018	6.819 ± 0.017	6.840 ± 0.062	6.827 ± 0.045	7.305 ± 0.062	7.230 ± 0.060	1,2,3,5
GJ 436	10.14 ± 0.24	6.1 ± 0.9*	−1.07 ± 0.35	6.900 ± 0.024	6.319 ± 0.023	6.073 ± 0.016	5.889 ± 0.031	5.836 ± 0.023	6.277 ± 0.062	6.265 ± 0.023	1,2,3,7
GJ 1214	14.55 ± 0.13	9.1 ± 4.4*	−0.2 ± 1.4	9.750 ± 0.024	9.094 ± 0.024	8.782 ± 0.020	8.488 ± 0.064	8.397 ± 0.060	–	–	1,3,4
55 Cnc	12.34 ± 0.11	12.2 ± 0.9	0.44 ± 0.17	4.768 ± 0.244	4.265 ± 0.234	4.015 ± 0.036*	4.09 ± 0.11	4.065 ± 0.062	–	–	1,2,3,5
TReS-1	–	129.7 ± 8.7	5.56 ± 0.15	10.294 ± 0.024	9.887 ± 0.021	9.819 ± 0.019	9.779 ± 0.047	9.779 ± 0.044	10.232 ± 0.049	10.241 ± 0.048	1,3,5
TReS-2	–	195.3 ± 12.0	6.45 ± 0.14	10.232 ± 0.020	9.920 ± 0.026	9.846 ± 0.022	9.782 ± 0.045	9.790 ± 0.043	10.206 ± 0.069	10.252 ± 0.070	1,3,5
TReS-3	–	258.5 ± 16.1	7.06 ± 0.14	11.015 ± 0.022	10.655 ± 0.020	10.608 ± 0.017	10.550 ± 0.064	10.599 ± 0.064	11.029 ± 0.076	11.03 ± 0.14	1,3,6
TReS-4	–	576.0 ± 56.7	8.80 ± 0.22	10.583 ± 0.018	10.350 ± 0.015	10.330 ± 0.019	10.264 ± 0.064	10.279 ± 0.063	10.700 ± 0.073	10.741 ± 0.074	1,3,5
XO-1	–	177.9 ± 10.7	6.25 ± 0.13	9.939 ± 0.022	9.601 ± 0.017	9.527 ± 0.015	9.465 ± 0.061	9.515 ± 0.061	9.947 ± 0.069	9.967 ± 0.075	1,3,5
XO-2	–	156.0 ± 8.8	5.97 ± 0.13	9.744 ± 0.022	9.340 ± 0.026	9.308 ± 0.021	9.236 ± 0.064	9.294 ± 0.060	9.725 ± 0.078	9.733 ± 0.072	1,3,5
XO-3	–	185.7 ± 11.8	6.34 ± 0.14	9.013 ± 0.029	8.845 ± 0.018	8.791 ± 0.019	8.754 ± 0.039	8.757 ± 0.037	9.210 ± 0.067	9.213 ± 0.067	1,3,5
XO-4	–	308.2 ± 19.6	7.44 ± 0.14	9.667 ± 0.021	9.476 ± 0.022	9.406 ± 0.023	9.386 ± 0.066	9.409 ± 0.061	–	–	1,3,5
HAT-P-1B	–	129.6 ± 5.9	5.56 ± 0.10	9.156 ± 0.026	8.923 ± 0.030	8.858 ± 0.018	8.875 ± 0.064	8.853 ± 0.065	9.278 ± 0.069	9.308 ± 0.072	1,3,7
HAT-P-2	114.3 ± 9.8	125.3 ± 13.1	5.49 ± 0.24	7.796 ± 0.027	7.652 ± 0.038	7.603 ± 0.020	7.544 ± 0.063	7.603 ± 0.043	8.075 ± 0.063	8.054 ± 0.062	1,2,3,5
HAT-P-3	–	166.4 ± 14.4	6.11 ± 0.20	9.936 ± 0.022	9.542 ± 0.028	9.448 ± 0.025	9.382 ± 0.065	9.450 ± 0.062	–	–	1,3,5
HAT-P-4	–	293.5 ± 19.4	7.34 ± 0.15	10.100 ± 0.022	9.837 ± 0.020	9.770 ± 0.020	9.749 ± 0.072	9.799 ± 0.068	–	–	1,3,5
HAT-P-6	–	277.8 ± 19.1	7.22 ± 0.15	9.558 ± 0.023	9.440 ± 0.018	9.313 ± 0.019	9.289 ± 0.067	9.301 ± 0.063	–	–	1,3,5
HAT-P-7	–	320.8 ± 17.4	7.53 ± 0.12	9.555 ± 0.030	9.344 ± 0.029	9.334 ± 0.018	9.291 ± 0.068	9.281 ± 0.043	9.727 ± 0.081	9.759 ± 0.068	1,3,5
HAT-P-8	–	227.8 ± 12.7	6.79 ± 0.12	9.214 ± 0.022	9.004 ± 0.018	8.953 ± 0.013	8.942 ± 0.064	8.932 ± 0.060	–	–	1,3,5
HAT-P-12	–	139.1 ± 9.6	5.72 ± 0.16	10.794 ± 0.023	10.236 ± 0.022	10.108 ± 0.016	10.084 ± 0.048	10.135 ± 0.047	–	–	1,3,7
HAT-P-23	–	355.0 ± 40.8	7.75 ± 0.27	11.103 ± 0.022	10.846 ± 0.022	10.791 ± 0.020	10.822 ± 0.066	10.770 ± 0.068	–	–	1,3,5
WASP-1	–	346.4 ± 34.8	7.70 ± 0.23	10.586 ± 0.019	10.364 ± 0.016	10.276 ± 0.018	10.234 ± 0.047	10.237 ± 0.044	10.65 ± 0.19	10.71 ± 0.13	1,3,5
WASP-2	–	153.9 ± 8.3	5.94 ± 0.12	10.166 ± 0.027	9.752 ± 0.026	9.632 ± 0.024	9.588 ± 0.066	9.606 ± 0.065	10.02 ± 0.11	10.032 ± 0.071	1,3,7
WASP-3	–	251.4 ± 18.8	7.00 ± 0.17	9.603 ± 0.020	9.407 ± 0.014	9.361 ± 0.015	9.366 ± 0.045	9.356 ± 0.063	9.773 ± 0.067	9.758 ± 0.072	1,3,5
WASP-4	–	280.9 ± 31.1	7.24 ± 0.25	11.179 ± 0.025	10.842 ± 0.026	10.746 ± 0.021	10.710 ± 0.051	10.732 ± 0.046	–	–	1,3,5
WASP-5	–	318.6 ± 19.9	7.52 ± 0.14	10.949 ± 0.022	10.650 ± 0.025	10.598 ± 0.023	10.539 ± 0.069	10.590 ± 0.072	–	–	1,3,7
WASP-8A	–	85.1 ± 10.7	4.65 ± 0.29	8.501 ± 0.027	8.218 ± 0.049	8.086 ± 0.023	8.084 ± 0.085	8.162 ± 0.077	–	8.552 ± 0.063	1,3,5
WASP-12A	–	436.3 ± 37.3	8.20 ± 0.19	10.477 ± 0.021	10.228 ± 0.022	10.188 ± 0.020	10.111 ± 0.042	10.100 ± 0.038	10.541 ± 0.074	10.55 ± 0.10	1,3,5
WASP-14	–	208.4 ± 15.9	6.60 ± 0.17	8.869 ± 0.021	8.650 ± 0.019	8.621 ± 0.019	8.586 ± 0.046	8.576 ± 0.043	–	9.034 ± 0.064	1,3,5
WASP-17	–	476.0 ± 36.0	8.39 ± 0.17	10.509 ± 0.027	10.319 ± 0.024	10.224 ± 0.027	10.196 ± 0.064	10.193 ± 0.065	10.66 ± 0.11	10.66 ± 0.11	1,3,5
WASP-18	99 ± 11	122.6 ± 6.7	5.44 ± 0.12	8.409 ± 0.018	8.231 ± 0.055	8.131 ± 0.027	8.098 ± 0.046	8.115 ± 0.044	8.561 ± 0.047	8.573 ± 0.063	1,2,3,5
WASP-19	–	275.9 ± 13.4	7.20 ± 0.11	10.911 ± 0.026	10.602 ± 0.022	10.481 ± 0.023	10.445 ± 0.047	10.486 ± 0.047	10.91 ± 0.13	10.754 ± 0.085	1,3,7
WASP-24	–	332.5 ± 23.8	7.61 ± 0.16	10.457 ± 0.022	10.219 ± 0.026	10.148 ± 0.023	10.132 ± 0.067	10.156 ± 0.066	–	–	1,3,5
WASP-26A	–	293.4 ± 20.5	7.34 ± 0.16	10.021 ± 0.022	9.775 ± 0.023	9.690 ± 0.023	9.680 ± 0.075	9.708 ± 0.067	–	–	1,4,5
WASP-33	116 ± 11	123.1 ± 7.2	5.45 ± 0.13	7.581 ± 0.021	7.516 ± 0.024	7.468 ± 0.024	7.427 ± 0.066	7.438 ± 0.060	–	–	1,2,3,5
WASP-43	–	106.1 ± 7.2	5.31 ± 0.24	9.995 ± 0.024	9.397 ± 0.025	9.267 ± 0.026	9.129 ± 0.063	9.214 ± 0.061	–	–	1,3,7
WASP-48	–	466.0 ± 49.0	8.34 ± 0.24	10.627 ± 0.025	10.441 ± 0.032	10.372 ± 0.022	10.340 ± 0.065	10.360 ± 0.069	–	–	1,3,5
CoRoT-1	–	715.2 ± 58.2	9.27 ± 0.18	12.462 ± 0.029	12.218 ± 0.026	12.149 ± 0.027	12.12 ± 0.12	12.114 ± 0.095	–	–	1,3,7
CoRoT-2A	–	255.0 ± 16.2	7.03 ± 0.14	10.783 ± 0.028	10.438 ± 0.037	10.310 ± 0.031	10.297 ± 0.071	10.309 ± 0.078	–	10.627 ± 0.072	1,3,7
Kepler-7	–	893.3 ± 50.5	9.76 ± 0.13	11.833 ± 0.020	11.601 ± 0.022	11.535 ± 0.020	11.545 ± 0.077	11.536 ± 0.074	–	–	1,3,7
KELT-1	–	251.3 ± 13.0	7.00 ± 0.12	9.682 ± 0.022	9.534 ± 0.030	9.437 ± 0.019	9.390 ± 0.063	9.405 ± 0.061	–	–	1,3,5

References: (1) this paper; (2) van Leeuwen (2007); (3) Cutri et al. (2003); (4) Anglada-Escudé et al. (2013); (5) Høg et al. (2000); (6) Droege et al. (2006); (7) Zacharias et al. (2013).
*Flagged in the 2MASS catalogue.

Table B3. Adopted distance and estimated stellar absolute magnitudes using data presented in Table B2, in the Vega-based magnitude convention.

Name	Adopted distance (pc)	Absolute magnitudes							
		M_V	M_J	M_H	M_{K_s}	$M_{[3.6]}$	$M_{[4.5]}$	$M_{[5.8]}$	$M_{[8.0]}$
HD 189733A	19.1 ± 1.0	6.27 ± 0.12	4.67 ± 0.12	4.18 ± 0.12	4.14 ± 0.11	4.04 ± 0.13	4.12 ± 0.13	4.57 ± 0.13	4.56 ± 0.13
HD 209458	49.0 ± 2.2	4.18 ± 0.10	3.140 ± 0.099	2.915 ± 0.099	2.86 ± 0.10	2.80 ± 0.11	2.85 ± 0.10	3.34 ± 0.11	3.31 ± 0.11
HD 80606	65.8 ± 3.9	4.91 ± 0.13	3.61 ± 0.13	3.31 ± 0.13	3.22 ± 0.13	3.17 ± 0.14	3.26 ± 0.13	–	3.65 ± 0.14
HD 149026	80.8 ± 4.0	3.60 ± 0.11	2.58 ± 0.11	2.36 ± 0.11	2.28 ± 0.11	2.30 ± 0.12	2.29 ± 0.12	2.77 ± 0.13	2.69 ± 0.13
GJ 436	10.14 ± 0.24	11.68 ± 0.35	6.870 ± 0.057	6.289 ± 0.056	6.043 ± 0.052	5.858 ± 0.063	5.806 ± 0.054	6.25 ± 0.082	6.235 ± 0.056
GJ 1214	14.55 ± 0.13	14.9 ± 1.4	8.936 ± 0.030	8.280 ± 0.031	7.968 ± 0.028	7.674 ± 0.065	7.58 ± 0.062	–	–
55 Cnc	12.2 ± 0.9	5.50 ± 0.17	4.33 ± 0.29	3.83 ± 0.29	3.58 ± 0.17	3.66 ± 0.19	3.63 ± 0.17	–	–
TReS-1	129.7 ± 8.7	5.86 ± 0.11	4.73 ± 0.14	4.32 ± 0.16	4.25 ± 0.15	4.21 ± 0.16	4.21 ± 0.16	4.67 ± 0.16	4.68 ± 0.15
TReS-2	195.3 ± 12.0	4.80 ± 0.11	3.78 ± 0.13	3.47 ± 0.14	3.39 ± 0.19	3.33 ± 0.14	3.34 ± 0.14	3.75 ± 0.15	3.80 ± 0.15
TReS-3	258.5 ± 16.1	5.33 ± 0.12	3.95 ± 0.14	3.59 ± 0.18	3.55 ± 0.14	3.49 ± 0.16	3.54 ± 0.15	3.97 ± 0.16	3.97 ± 0.19
TReS-4	576.0 ± 56.7	3.13 ± 0.16	1.78 ± 0.21	1.55 ± 0.22	1.53 ± 0.22	1.46 ± 0.23	1.48 ± 0.22	1.90 ± 0.23	1.94 ± 0.23
XO-1	177.9 ± 10.7	5.00 ± 0.12	3.69 ± 0.13	3.35 ± 0.13	3.28 ± 0.13	3.21 ± 0.15	3.26 ± 0.15	3.70 ± 0.15	3.72 ± 0.16
XO-2	156.0 ± 8.8	5.28 ± 0.10	3.78 ± 0.13	3.37 ± 0.14	3.34 ± 0.13	3.27 ± 0.14	3.33 ± 0.14	3.76 ± 0.14	3.77 ± 0.14
XO-3	185.7 ± 11.8	3.51 ± 0.14	2.67 ± 0.14	2.50 ± 0.14	2.45 ± 0.14	2.41 ± 0.15	2.41 ± 0.15	2.87 ± 0.15	2.87 ± 0.15
XO-4	308.2 ± 19.6	3.37 ± 0.13	2.22 ± 0.13	2.03 ± 0.14	1.96 ± 0.14	1.94 ± 0.15	1.96 ± 0.16	–	–
HAT-P-1B	129.6 ± 5.9	4.31 ± 0.10	3.59 ± 0.10	3.36 ± 0.10	3.29 ± 0.10	3.31 ± 0.12	3.29 ± 0.12	3.71 ± 0.12	3.74 ± 0.12
HAT-P-2	125.3 ± 13.1	3.20 ± 0.24	2.30 ± 0.23	2.16 ± 0.23	2.11 ± 0.24	2.05 ± 0.24	2.11 ± 0.24	2.59 ± 0.24	2.56 ± 0.24
HAT-P-3	166.4 ± 14.4	5.75 ± 0.13	3.83 ± 0.20	3.44 ± 0.18	3.34 ± 0.18	3.28 ± 0.20	3.34 ± 0.20	–	–
HAT-P-4	293.5 ± 19.4	3.78 ± 0.13	2.76 ± 0.15	2.50 ± 0.14	2.43 ± 0.15	2.41 ± 0.16	2.46 ± 0.16	–	–
HAT-P-6	277.8 ± 19.1	3.25 ± 0.15	2.34 ± 0.15	2.22 ± 0.15	2.09 ± 0.15	2.07 ± 0.16	2.08 ± 0.16	–	–
HAT-P-7	320.8 ± 17.4	2.95 ± 0.11	2.02 ± 0.12	1.81 ± 0.12	1.80 ± 0.12	1.76 ± 0.13	1.75 ± 0.13	2.20 ± 0.14	2.23 ± 0.14
HAT-P-8	227.8 ± 12.7	3.57 ± 0.12	2.43 ± 0.12	2.22 ± 0.12	2.17 ± 0.13	2.15 ± 0.14	2.14 ± 0.14	–	–
HAT-P-12	139.1 ± 9.6	7.05 ± 0.15	5.08 ± 0.15	4.52 ± 0.15	4.39 ± 0.15	4.37 ± 0.16	4.42 ± 0.16	–	–
HAT-P-23	355.0 ± 40.8	4.31 ± 0.18	3.35 ± 0.26	3.09 ± 0.26	3.04 ± 0.26	3.07 ± 0.27	3.02 ± 0.25	–	3.01 ± 0.26
WASP-1	346.4 ± 34.8	3.61 ± 0.19	2.89 ± 0.22	2.67 ± 0.22	2.58 ± 0.23	2.54 ± 0.21	2.54 ± 0.23	2.95 ± 0.30	–
WASP-2	153.9 ± 8.3	5.88 ± 0.12	4.23 ± 0.18	3.82 ± 0.12	3.70 ± 0.12	3.65 ± 0.13	3.67 ± 0.14	4.08 ± 0.18	4.10 ± 0.13
WASP-3	251.4 ± 18.8	3.63 ± 0.16	2.60 ± 0.17	2.40 ± 0.16	2.36 ± 0.16	2.36 ± 0.17	2.35 ± 0.17	2.77 ± 0.18	2.76 ± 0.18
WASP-4	280.9 ± 31.1	5.24 ± 0.11	3.94 ± 0.24	3.60 ± 0.25	3.50 ± 0.24	3.47 ± 0.26	3.49 ± 0.25	–	–
WASP-5	318.6 ± 19.9	4.63 ± 0.14	3.43 ± 0.14	3.13 ± 0.14	3.08 ± 0.14	3.02 ± 0.15	3.07 ± 0.15	–	–
WASP-8A	85.1 ± 10.7	5.14 ± 0.29	3.85 ± 0.28	3.57 ± 0.28	3.44 ± 0.28	3.43 ± 0.30	3.51 ± 0.29	–	3.90 ± 0.28
WASP-12A	436.3 ± 37.3	3.37 ± 0.11	2.28 ± 0.19	2.03 ± 0.19	1.99 ± 0.20	1.91 ± 0.20	1.90 ± 0.19	2.34 ± 0.20	2.35 ± 0.21
WASP-14	208.4 ± 15.9	3.15 ± 0.17	2.27 ± 0.17	2.06 ± 0.17	2.03 ± 0.17	1.99 ± 0.17	1.96 ± 0.17	–	2.44 ± 0.18
WASP-17	476.0 ± 36.0	3.20 ± 0.13	2.12 ± 0.17	1.93 ± 0.17	1.84 ± 0.16	1.81 ± 0.18	1.80 ± 0.17	–	2.27 ± 0.20
WASP-18	122.6 ± 6.7	3.86 ± 0.12	2.97 ± 0.12	2.79 ± 0.13	2.69 ± 0.13	2.66 ± 0.13	2.67 ± 0.13	3.12 ± 0.14	3.13 ± 0.13
WASP-19	275.9 ± 13.4	5.11 ± 0.10	3.70 ± 0.11	3.40 ± 0.10	3.28 ± 0.11	3.24 ± 0.12	3.28 ± 0.12	3.71 ± 0.17	3.55 ± 0.13
WASP-24	332.5 ± 23.8	3.61 ± 0.12	2.85 ± 0.16	2.61 ± 0.16	2.54 ± 0.16	2.52 ± 0.17	2.55 ± 0.16	–	–
WASP-26A	293.4 ± 20.5	3.96 ± 0.12	2.68 ± 0.15	2.44 ± 0.15	2.35 ± 0.15	2.34 ± 0.17	2.37 ± 0.17	–	–
WASP-33	123.1 ± 7.2	2.69 ± 0.13	2.13 ± 0.13	2.06 ± 0.13	2.02 ± 0.13	1.98 ± 0.14	1.99 ± 0.14	–	–
WASP-43	106.1 ± 7.2	7.36 ± 0.23	4.87 ± 0.15	4.27 ± 0.15	4.14 ± 0.15	4.00 ± 0.15	4.08 ± 0.16	–	–
WASP-48	466.0 ± 49.0	3.38 ± 0.20	2.29 ± 0.23	2.10 ± 0.24	2.03 ± 0.23	2.00 ± 0.24	2.02 ± 0.24	–	3.59 ± 0.16
CoRoT-1	715.2 ± 58.2	4.29 ± 0.18	3.19 ± 0.18	2.95 ± 0.18	2.88 ± 0.17	2.85 ± 0.21	2.84 ± 0.21	–	–
CoRoT-2A	255.0 ± 16.2	5.25 ± 0.11	3.75 ± 0.14	3.41 ± 0.14	3.28 ± 0.14	3.26 ± 0.16	3.28 ± 0.16	–	–
Kepler-7	893.3 ± 50.5	3.25 ± 0.12	2.08 ± 0.12	1.85 ± 0.12	1.78 ± 0.12	1.79 ± 0.15	1.78 ± 0.14	–	–
KELT-1	251.3 ± 13.0	3.70 ± 0.10	2.68 ± 0.12	2.53 ± 0.12	2.44 ± 0.11	2.39 ± 0.13	2.40 ± 0.13	–	–

Table B4. Apparent magnitudes for the dayside of occulting extrasolar planets in the *Vega*-based magnitude convention. References in the last column include the discovery paper and the published flux drop at occultation. List compiled with the help of exoplanets.org (Wright et al. 2011) and of the SAO/NASA ADS paper repository.

Name	Distance modulus $(m - M)$	Apparent magnitudes m_J	m_H	m_{K_s}	$m_{[3.6]}$	$m_{[4.5]}$	$m_{[5.8]}$	$m_{[8.0]}$	Refs
HD 189733A b	1.41 ± 0.12	–	–	–	12.532 ± 0.070	12.400 ± 0.064	12.24 ± 0.13	11.680 ± 0.071	1,2,3
HD 209458 b	3.45 ± 0.10	–	–	–	13.83 ± 0.11	12.984 ± 0.083	13.09 ± 0.17	13.31 ± 0.13	1,4,5,6,7
HD 80606 b	4.09 ± 0.13	–	–	–	–	–	–	15.24 ± 0.23	1,8,9
HD 149026 b	4.54 ± 0.11	–	–	–	15.33 ± 0.10	15.50 ± 0.20	15.70 ± 0.27	15.44 ± 0.14	1,10,11
GJ 436 b	−1.07 ± 0.35	–	–	–	15.27 ± 0.28	>15.8	15.4 ± 1.1	14.868 ± 0.093	1,12,13,14
GJ 1214 b	−0.2 ± 1.4	–	–	–	>17.7	>17.7	–	–	1,15,16
55 Cnc e	0.44 ± 0.17	–	–	–	–	13.77 ± 0.27	–	–	1,17,18,19,20,21
TReS-1 b	5.56 ± 0.15	–	–	–	–	17.73 ± 0.23	–	16.86 ± 0.18	1,22,23
TReS-2 b	6.45 ± 0.14	–	–	17.86 ± 0.23	17.02 ± 0.20	16.39 ± 0.12	16.96 ± 0.37	16.36 ± 0.20	1,24,25,26
TReS-3 b	7.06 ± 0.14	–	>18.9	17.80 ± 0.15	16.70 ± 0.12	16.67 ± 0.18	16.90 ± 0.27	16.84 ± 0.18	1,27,28,29
TReS-4 b	8.80 ± 0.22	–	–	–	17.42 ± 0.11	17.35 ± 0.13	17.36 ± 0.34	16.98 ± 0.17	1,30,31
XO-1 b	6.25 ± 0.13	–	–	–	17.13 ± 0.11	16.80 ± 0.11	16.41 ± 0.15	16.66 ± 0.17	1,32,33
XO-2 b	5.97 ± 0.13	–	–	–	16.96 ± 0.24	16.82 ± 0.24	16.67 ± 0.26	16.92 ± 0.52	1,34,35
XO-3 b	6.34 ± 0.14	–	–	–	16.24 ± 0.059	15.869 ± 0.058	16.39 ± 0.53	16.27 ± 0.30	1,36,37
XO-4 b	7.44 ± 0.14	–	–	16.26 ± 0.27	17.52 ± 0.26	16.58 ± 0.10	–	–	1,38,39
HAT-P-1B b	5.56 ± 0.10	–	–	–	16.62 ± 0.12	16.03 ± 0.20	16.01 ± 0.18	15.87 ± 0.20	1,40,41,42
HAT-P-2 b	5.49 ± 0.24	–	–	–	15.05 ± 0.096	15.07 ± 0.079	15.95 ± 0.68	15.19 ± 0.10	1,43,44
HAT-P-3 b	6.11 ± 0.20	–	–	–	16.76 ± 0.32	17.02 ± 0.20	–	–	1,45,46
HAT-P-4 b	7.34 ± 0.15	–	–	–	16.87 ± 0.15	17.08 ± 0.15	–	–	1,47,46
HAT-P-6 b	7.22 ± 0.15	–	–	–	16.62 ± 0.10	16.738 ± 0.087	–	–	1,48,39
HAT-P-7 b	7.53 ± 0.12	–	–	–	16.81 ± 0.21	16.28 ± 0.16	16.25 ± 0.16	16.38 ± 0.27	1,49,50
HAT-P-8 b	6.79 ± 0.12	–	–	–	16.15 ± 0.10	16.319 ± 0.097	–	–	1,51,39
HAT-P-12 b	5.72 ± 0.16	–	–	–	>18.5	17.8	–	–	1,52,46
HAT-P-23 b	7.75 ± 0.27	–	–	–	17.34 ± 0.10	17.05 ± 0.11	–	–	1,53,54
WASP-1 b	7.70 ± 0.23	–	–	–	17.07 ± 0.10	16.896 ± 0.099	17.06 ± 0.30	16.52 ± 0.17	1,55,56

Table B4 – *continued*

Name	Distance modulus (m − M)	m_J	m_H	m_{K_s}	Apparent magnitudes $m_{[3.6]}$	$m_{[4.5]}$	$m_{[5.8]}$	$m_{[8.0]}$	Refs
WASP-2 b	5.94 ± 0.12	–	–	–	17.29 ± 0.69	16.54 ± 0.13	16.81 ± 0.63	16.39 ± 0.27	1,55,56
WASP-3 b	7.00 ± 0.17	–	–	16.27 ± 0.18	–	–	–	–	1,57,58
WASP-4 b	7.24 ± 0.25	–	–	17.58 ± 0.13	16.95 ± 0.12	16.894 ± 0.095	–	–	1,59,60,61
WASP-5 b	7.52 ± 0.14	–	–	–	17.10 ± 0.13	17.35 ± 0.17	–	–	1,62,63
WASP-8A b	4.65 ± 0.29	–	–	–	15.45 ± 0.20	16.06 ± 0.14	–	16.13 ± 0.31	1,64,65
WASP-12A b	8.20 ± 0.19	17.62 ± 0.24	17.03 ± 0.17	16.363 ± 0.050	16.056 ± 0.053	16.032 ± 0.065	15.94 ± 0.12	15.94 ± 0.15	1,66,67
WASP-14 b	6.60 ± 0.17	–	–	–	15.406 ± 0.060	15.18 ± 0.10	–	15.89 ± 0.14	1,68,69
WASP-17 b	8.39 ± 0.17	–	–	–	–	16.793 ± 0.089	–	17.22 ± 0.21	1,70,71
WASP-18 b	5.44 ± 0.12	–	–	–	14.405 ± 0.088	14.166 ± 0.072	14.641 ± 0.099	14.541 ± 0.081	1,72,73,74
WASP-19 b	7.20 ± 0.11	–	17.00 ± 0.19	–	16.235 ± 0.072	16.094 ± 0.075	16.38 ± 0.23	16.10 ± 0.21	1,75,76
WASP-24 b	7.61 ± 0.16	–	–	–	17.13 ± 0.11	16.89 ± 0.12	–	–	1,77,78
WASP-26A b	7.34 ± 0.16	–	–	–	16.93 ± 0.14	16.78 ± 0.13	–	–	1,79,80
WASP-33 b	5.45 ± 0.13	–	–	14.00 ± 0.12	13.89 ± 0.23	13.406 ± 0.082	–	–	1,81,82,83
WASP-43 b	5.31 ± 0.24	–	16.80 ± 0.17	16.05 ± 0.17	15.281 ± 0.077	15.26 ± 0.074	–	–	1,84,85,86
WASP-48 b	8.34 ± 0.24	–	–	–	17.22 ± 0.11	17.03 ± 0.12	–	–	1,87,54
CoRoT-1 b	9.27 ± 0.18	–	19.31 ± 0.44	18.33 ± 0.15	18.07 ± 0.16	17.91 ± 0.13	–	–	1,88,89,90,91
CoRoT-2A b	7.03 ± 0.14	–	–	17.3 ± 1.2	16.421 ± 0.092	16.062 ± 0.087	–	16.36 ± 0.14	1,92,89
Kepler-7 b	9.76 ± 0.13	–	–	–	>19.6	>19.0	–	–	1,94,95
KELT-1 b	7.00 ± 0.12	–	–	–	16.165 ± 0.085	16.152 ± 0.089	–	–	1,96,97

References: (1) this paper; (2) Bouchy et al. (2005); (3) Knutson et al. (2012); (4) Charbonneau et al. (2000); (5) Henry et al. (2000); (6) Mazeh et al. (2000); (7) Knutson et al. (2008); (8) Naef et al. (2001); (9) Laughlin et al. (2009); (10) Sato et al. (2005); (11) Stevenson et al. (2012); (12) Butler et al. (2004); (13) Gillon et al. (2007); (14) Lanotte et al. (in preparation); (15) Charbonneau et al. (2009); (16) Gillon et al. (2014); (17) McArthur et al. (2004); (18) Dawson & Fabrycky (2010); (19) Winn et al. (2011); (20) Demory et al. (2011); (21) Demory et al. (2012); (22) Alonso et al. (2004); (23) Charbonneau et al. (2005); (24) O'Donovan et al. (2006); (25) O'Donovan et al. (2010); (26) Croll et al. (2010a); (27) O'Donovan et al. (2007); (28) Fressin et al. (2010); (29) Croll et al. (2010b); (30) Mandushev et al. (2007); (31) Knutson et al. (2009); (32) McCullough et al. (2006); (33) Machalek et al. (2008); (34) Burke et al. (2007); (35) Johns-Krull et al. (2008); (36) Machalek et al. (2010); (37) Machalek et al. (2008); (38) McCullough et al. (2008); (39) Todorov et al. (2012); (40) Bakos et al. (2007a); (41) Todorov et al. (2010); (42) de Mooij et al. (2011); (43) Bakos et al. (2007b); (44) Lewis et al. (2013); (45) Torres et al. (2007); (46) Todorov et al. (2013); (47) Kovács et al. (2007); (48) Noyes et al. (2008); (49) Pál et al. (2008); (50) Christiansen et al. (2010); (51) Latham et al. (2009); (52) Hartman et al. (2009); (53) Bakos et al. (2011); (54) O'Rourke et al. (2014); (55) Collier Cameron et al. (2007); (56) Wheatley et al. (2010); (57) Pollacco et al. (2008); (58) Zhao et al. (2012b); (59) Wilson et al. (2008); (60) Beerer et al. (2011); (61) Cáceres et al. (2011); (62) Anderson et al. (2008); (63) Baskin et al. (2013); (64) Queloz et al. (2010); (65) Cubillos et al. (2013); (66) Hebb et al. (2009); (67) Crossfield et al. (2012); (68) Joshi et al. (2009); (69) Blecic et al. (2013); (70) Anderson et al. (2010); (71) Anderson et al. (2011a); (72) Hellier et al. (2009); (73) Nymeyer et al. (2011); (74) Maxted et al. (2013); (75) Hebb et al. (2010); (76) Anderson et al. (2013); (77) Street et al. (2010); (78) Smith et al. (2012); (79) Smalley et al. (2010); (80) Mahtani et al. (2013); (81) Collier Cameron et al. (2010); (82) Deming et al. (2012); (83) de Mooij et al. (2013); (84) Hellier et al. (2011); (85) Blecic et al. (2014); (86) Wang et al. (2013); (87) Enoch et al. (2011); (88) Barge et al. (2008); (89) Deming et al. (2011); (90) Rogers et al. (2009); (91) Zhao et al. (2012a); (92) Alonso et al. (2008); (93) Alonso et al. (2010); (94) Latham et al. (2010); (95) Demory et al. (2013); (96) Siverd et al. (2012); (97) Beatty et al. (2014).

Table B5. Absolute magnitudes for the dayside of occulting extrasolar planets in the Vega-based magnitude convention.

Name	Absolute magnitudes						
	M_J	M_H	M_{K_s}	$M_{[3.6]}$	$M_{[4.5]}$	$M_{[5.8]}$	$M_{[8.0]}$
HD 189733A b	–	–	–	11.13 ± 0.14	11.00 ± 0.13	10.83 ± 0.18	10.27 ± 0.14
HD 209458 b	–	–	–	10.37 ± 0.15	9.53 ± 0.13	9.64 ± 0.20	9.86 ± 0.17
HD 80606 b	–	–	–	–	–	–	11.15 ± 0.28
HD 149026 b	–	–	–	10.80 ± 0.15	10.96 ± 0.23	11.16 ± 0.31	10.90 ± 0.18
GJ 436 b	–	–	–	15.24 ± 0.28	>15.8	15.3 ± 1.1	14.84 ± 0.10
GJ 1214 b	–	–	–	>16.9	>16.9	–	–
55 Cnc e	–	–	–	–	13.34 ± 0.31	–	–
TReS-1 b	–	–	–	–	12.17 ± 0.29	–	11.30 ± 0.23
TReS-2 b	–	–	11.41 ± 0.25	10.57 ± 0.24	9.93 ± 0.18	10.51 ± 0.36	9.91 ± 0.24
TReS-3 b	–	>11.8	10.74 ± 0.20	9.64 ± 0.20	9.61 ± 0.22	9.84 ± 0.31	9.78 ± 0.23
TReS-4 b	–	–	–	8.62 ± 0.25	8.55 ± 0.25	8.56 ± 0.42	8.18 ± 0.27
XO-1 b	–	–	–	10.88 ± 0.17	10.55 ± 0.17	10.15 ± 0.19	10.41 ± 0.22
XO-2 b	–	–	–	11.00 ± 0.29	10.85 ± 0.27	10.70 ± 0.30	10.96 ± 0.52
XO-3 b	–	–	–	9.90 ± 0.15	9.52 ± 0.16	10.05 ± 0.54	9.93 ± 0.34
XO-4 b	–	–	–	10.07 ± 0.29	9.14 ± 0.18	–	–
HAT-P-1B b	–	–	10.70 ± 0.31	11.05 ± 0.16	10.46 ± 0.22	10.44 ± 0.20	10.30 ± 0.22
HAT-P-2 b	–	–	–	9.56 ± 0.26	9.58 ± 0.25	10.46 ± 0.72	9.71 ± 0.25
HAT-P-3 b	–	–	–	10.65 ± 0.38	10.91 ± 0.27	–	–
HAT-P-4 b	–	–	–	9.53 ± 0.20	9.75 ± 0.20	–	–
HAT-P-6 b	–	–	–	9.40 ± 0.19	9.52 ± 0.17	–	–
HAT-P-7 b	–	–	–	9.28 ± 0.23	8.75 ± 0.20	8.72 ± 0.20	8.85 ± 0.34
HAT-P-8 b	–	–	–	9.36 ± 0.16	9.53 ± 0.16	–	–
HAT-P-12 b	–	–	–	>12.8	>12.1	–	–
HAT-P-23 b	–	–	–	9.58 ± 0.28	9.29 ± 0.27	–	–
WASP-1 b	–	–	–	9.37 ± 0.24	9.20 ± 0.24	9.36 ± 0.38	8.82 ± 0.28
WASP-2 b	–	–	–	11.35 ± 0.72	10.60 ± 0.18	10.88 ± 0.58	10.46 ± 0.28
WASP-3 b	–	–	9.21 ± 0.20	–	–	–	–
WASP-4 b	–	–	10.34 ± 0.27	9.71 ± 0.28	9.65 ± 0.27	–	–
WASP-5 b	–	–	–	9.59 ± 0.19	9.84 ± 0.22	–	–
WASP-8A b	–	–	–	10.80 ± 0.35	11.41 ± 0.31	–	11.48 ± 0.40
WASP-12A b	9.42 ± 0.32	8.83 ± 0.22	8.16 ± 0.20	7.86 ± 0.20	7.83 ± 0.20	7.74 ± 0.22	7.74 ± 0.24
WASP-14 b	–	–	–	8.81 ± 0.17	8.59 ± 0.19	–	9.30 ± 0.22
WASP-17 b	–	–	–	–	8.40 ± 0.18	–	8.84 ± 0.27
WASP-18 b	–	–	–	8.96 ± 0.15	8.72 ± 0.14	9.20 ± 0.17	9.10 ± 0.14
WASP-19 b	–	9.80 ± 0.21	–	9.03 ± 0.13	8.89 ± 0.13	9.17 ± 0.25	8.89 ± 0.24
WASP-24 b	–	–	–	9.52 ± 0.19	9.28 ± 0.18	–	–
WASP-26A b	–	–	–	9.59 ± 0.21	9.43 ± 0.20	–	–
WASP-33 b	–	–	8.55 ± 0.18	8.44 ± 0.25	7.95 ± 0.15	–	–
WASP-43 b	–	11.67 ± 0.23	10.92 ± 0.23	10.15 ± 0.16	10.13 ± 0.17	–	–
WASP-48 b	–	–	–	8.88 ± 0.25	8.69 ± 0.26	–	–
CoRoT-1 b	–	10.04 ± 0.52	9.06 ± 0.23	8.80 ± 0.24	8.63 ± 0.23	–	–
CoRoT-2A b	–	–	10.3 ± 1.1	9.39 ± 0.17	9.02 ± 0.17	–	9.33 ± 0.21
Kepler-7 b	–	–	–	>9.8	>9.3	–	–
KELT-1 b	–	–	–	9.16 ± 0.14	9.15 ± 0.14	–	–

This paper has been typeset from a TeX/LaTeX file prepared by the author.